

# Master's thesis

Evaluation of performance of an 80 l radon detector and radon adsorption efficiency of activated carbon fiber using  $\text{CF}_4$

2022 / 2 / 4

Department of Physics

201s109s

KOTSAR YURII

Kobe University Graduate School of Science

## Abstract

The radioactive noble gas radon-222 ( $^{222}\text{Rn}$ ) is a significant background source in many dark matter search experiments, such as the NEWAGE experiment, which employs tetrafluoromethane ( $\text{CF}_4$ ) gas at about 0.01 MPa. In this type of experiments, high accuracy, and low background level are crucial for any statistical significance. Thus a well-calibrated  $^{222}\text{Rn}$  detector with the ability to measure concentrations of  $< 1 \text{ mBq/m}^3$  is needed. Previously, quantitative analysis for a  $^{222}\text{Rn}$  detector has been performed with air, argon and xenon gases, but not with  $\text{CF}_4$ . To evaluate an 80 liter  $^{222}\text{Rn}$  detector's performance, the calibration factor was measured and its dependence on absolute humidity,  $^{222}\text{Rn}$  concentration and pressure analyzed. Significant dependencies on humidity and pressure were found. Additionally, activated carbon fibers have been employed to evaluate their radon adsorption efficiency in  $\text{CF}_4$  at 0.4 standard liter per minute. It was found to be  $82.7 \pm 0.1(\text{stat.}) \pm 2.3(\text{syst.})\%$  at 0.10 MPa. For pressures lower than atmospheric pressure (1–0.03 MPa), they have been seen to rise steadily, up to  $93.7 \pm 0.3(\text{stat.}) \pm 3.9(\text{syst.})\%$  at 0.03 MPa.

# Contents

<b>Preface</b>	<b>4</b>
<b>1 Dark matter</b>	<b>5</b>
1.1 Theoretical derivation . . . . .	5
1.2 Dark matter detection . . . . .	6
1.3 NEWAGE experiment . . . . .	7
<b>2 Radon background in underground dark matter experiments</b>	<b>8</b>
2.1 Radon gas . . . . .	8
2.2 Radon detectors . . . . .	8
2.3 Removal methods . . . . .	8
<b>3 An 80 l radon detection system</b>	<b>10</b>
3.1 Radon detector . . . . .	10
3.2 Detection principle . . . . .	11
3.3 Experimental setup . . . . .	12
<b>4 Calibration of the radon detector filled with CF<sub>4</sub></b>	<b>14</b>
4.1 Fundamentals . . . . .	14
4.1.1 Tetrafluoromethane . . . . .	14
4.1.2 Calibration factor . . . . .	14
4.1.3 Neutralization rate . . . . .	14
4.1.4 Absolute humidity . . . . .	15
4.2 Absolute humidity dependence . . . . .	15
4.3 Radon concentration dependence . . . . .	19
4.4 Background run . . . . .	21
<b>5 Measurement of radon adsorption efficiency of ACF</b>	<b>23</b>
5.1 Activated carbon fiber . . . . .	23
5.2 Cold trap . . . . .	24
5.3 Radon adsorption efficiency at atmospheric pressure . . . . .	24
5.4 Pressure dependence of radon adsorption efficiency . . . . .	28
5.5 Systematic uncertainties . . . . .	34
<b>6 Discussion and results</b>	<b>37</b>
6.1 Calibration factor's dependence on absolute humidity . . . . .	37
6.2 Pressure dependence of calibration factor . . . . .	37
6.3 Radon adsorption efficiency of ACF . . . . .	38
<b>7 Conclusion</b>	<b>40</b>
<b>References</b>	<b>40</b>

# Preface

This study is a continuation of the paper “Evaluation of radon adsorption efficiency of activated carbon fiber using tetrafluoromethane” [1], published in the journal Progress of Theoretical and Experimental Physics in January 2022, which I worked on throughout my Master’s course at Kobe University. This study features a new introduction, extends and clarifies some explanations in the experimental part, and offers three new sections in the experimental part: *Radon concentration dependence* (Sect. 4.3) - for the calibration factor, *Systematic uncertainties* (Sect. 5.5) - for the radon adsorption efficiency, and *Pressure dependence of calibration factor* (Sect. 6.2) - in Discussion and results.

I would like to give my gratitude to my scientific advisor, Y. Takeuchi, for his rigorous supervision, which has not only made sure my research is done on time and to the highest standards, but has also helped me mature as a responsible member of society, and learn to not delay or neglect my tasks. He has also watched over me in my university life as a foreign student these 2 years, and has introduced me to different Japanese conferences on physics. I owe just as much to another advisor, and a collaborator on the original paper, Y. Nakano. I thank him for the many Zoom calls we had to discuss my research, and for his thorough yet rational advise on writing a scientific paper.

This work was supported by Japan Society for the Promotion of Science (JSPS) KAKENHI Grant Numbers 26104005, 26104008, 18H05536, 19H05806, 21K13942.

# 1 Dark matter

The dark matter is a predicted type of non-luminous matter, which fills most of the observable universe, and also accounts for around 26% of the energy distributed in the universe (Figure 1). It does not appear to interact via the electromagnetic field, and its gravitational interaction mode is also different from the gravitation as described by the Standard Model. This means that dark matter is difficult to detect and ascertain the presence of. As such, it has been a subject of speculation among physicists since more than 80 years ago.

This means that dark matter also does not interact with itself, since it seems structurally stable in permeating the galaxies. It could, however, allow for some new modes of self-interaction.

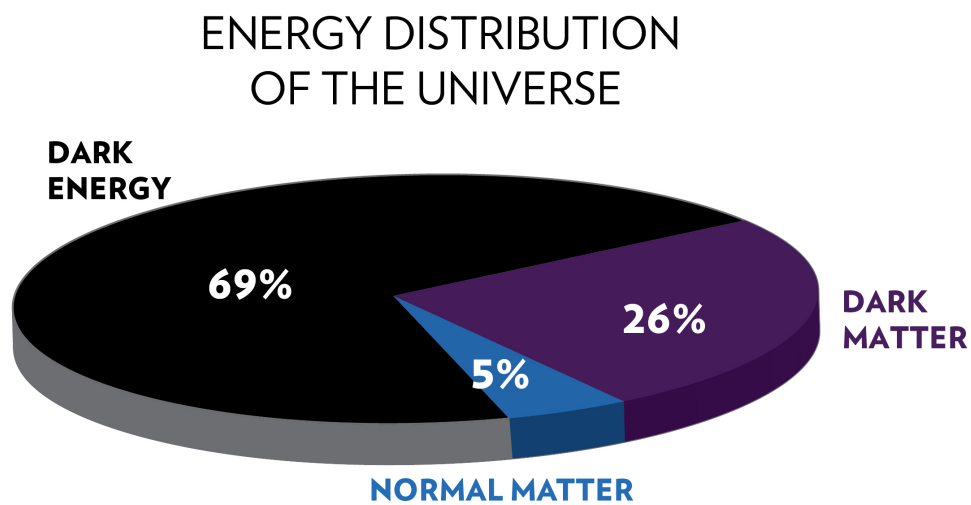


Figure 1: Estimates of the energy distribution in the universe [2].

## 1.1 Theoretical derivation

Dark matter was first used to explain mass discrepancies of astronomical bodies. Commonly, motions of other bodies around or within the object under study are used to directly determine its mass. Historically, mass discrepancies often arose when comparing different methods to estimate masses in astronomy.

In 1933, Fritz Zwicky, a Swiss astrophysicist, discovered that the redshifts of individual galaxies throughout the Coma cluster were much higher than the average, estimated from the total mass of the cluster. This meant that unless there was some form of non-luminous heavy matter keeping the clusters together, they would have long followed the

rapid expansion. Zwicky calculated that the Coma cluster is approximately 400 times more massive than visually observable.

The following 30 years, more data was collected that correlated with Zwicky's observations, and in 1978 (Rubin et al.; Bosma), as well as 1980 (Rubin et al.), spectrographic data confirmed that the rotation curves of galaxies at large galactocentric distances are approximately flat [3].

Nowadays, dark matter detection is one of the most sought after accomplishments in physics. To that end, there exist dozens of experiments worldwide which employ various detection methods.

## 1.2 Dark matter detection

Nowadays, various approaches are used to detect dark matter in a mass range, which spans 10 orders of magnitude. These approaches can be classified into direct searches, indirect searches and collider experiments. In recent years, however, the possible mass range for dark matter particle models has been refined extensively, and evidence points more in favor of cold dark matter [4, 5]. The weakly interacting massive particles (WIMPs) are one of the candidates for cold dark matter. WIMPs are well motivated by cosmological findings [6, 7] and supported by supersymmetry models, along with universal extra dimension and little Higgs models [8, 9, 10]. In theories with WIMPs, their direct detection is achieved by looking for elastic WIMP-nuclei scatterings or WIMP-electron scatterings. For example, the XENON experiment, which consists of a time projection chamber with dual-phase xenon (Xe), set a world-leading constraint ( $4.1 \times 10^{-47}$  cm<sup>2</sup> at 30 GeV) on the spin independent elastic scattering cross-section in 2018 [11]. The expected event rate for these interactions is extremely low due to the small scattering cross-section, and accordingly, in order to distinguish these signals from the background, an additional characteristic signal other than the simple energy spectrum is needed. To that end, some dark matter experiments search for the annual modulation of the event rate of aforementioned scatterings from the rotation of the Earth around the Sun, assuming dark matter has a uniform distribution throughout the Solar System. However, even these sets of data are not enough to prove to be consistent among different dark matter search experiments. Another method is then required to obtain more robust evidence.

### 1.3 NEWAGE experiment

One such method is to measure the WIMP-nuclei scatterings relative to the solar system’s movement in the galaxy. If dark matter truly permeates the Milky Way, we would expect a flow of dark matter particles from the direction of the Cygnus constellation, which is in the forward direction of the solar system’s motion around the galactic center. The NEWAGE (NEw generation WIMP search with an Advanced Gaseous tracking device Experiment) experiment [12] is a direct dark matter search experiment located at the Kamioka Observatory, the Institute for Cosmic Ray Research (ICRR), the University of Tokyo. NEWAGE is led by a team of researchers from Kobe University. The experiment searches for a difference in recoil angle between events in the direction of the Cygnus constellation and the opposite direction (Figure 2). It is hence a direction-sensitive experiment, and employs a gaseous three-dimensional fine tracking device (micro-TPC), which has a two-dimensional readout array, called the Micro Pixel Chamber ( $\mu$ -PIC) [13, 14]. A gas electron multiplier is positioned above the  $\mu$ -PIC and helps to reach the intensity for readout [15].

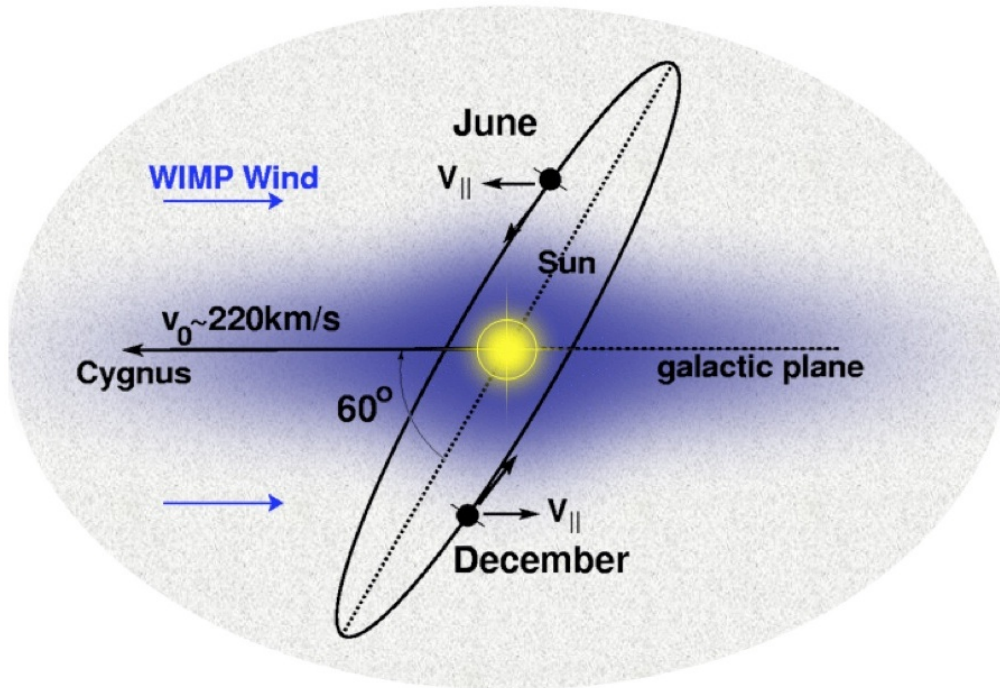


Figure 2: The NEWAGE experiment measures the dark matter flux (“dark matter wind”) in the direction of the Cygnus constellation, as compared to only measuring the annual variation of the event rate in other experiments. [16].

## 2 Radon background in underground dark matter experiments

### 2.1 Radon gas

In rare event search experiments, the background events from radioactive contaminants must be kept at a considerably low level. Such background sources include the noble gas in the uranium series radon-222 ( $^{222}\text{Rn}$ ), which has a half-life of 3.82 days and is produced continuously from trace amounts of radium-226 ( $^{226}\text{Ra}$ ) in the detector material. Due to its relatively long half-life, some of it persists in the experiment and can mimic signals in the analysis sensitive region. Therefore, the removal of  $^{222}\text{Rn}$  is a high priority in this class of experiments.

### 2.2 Radon detectors

To that end, a  $^{222}\text{Rn}$  detector is first needed to measure  $^{222}\text{Rn}$  concentration with high accuracy and precision, since rare event search experiments usually require considerably low  $^{222}\text{Rn}$  concentrations. Although in this type of experiments, measurements of  $< 1 \text{ mBq/m}^3$  are required, there are currently no commercially available Rn detectors, and so a special  $^{222}\text{Rn}$  detector has been developed for this purpose [17].

Since this type of experiments involves high accuracy measurements, it is necessary to account for any dependent behavior in the Rn detector, to consistently monitor the background level in its carrier gas. That includes the functional dependence of conversion factors between the measured variables and  $^{222}\text{Rn}$  concentration on those variable and/or external parameters. Furthermore, a typical Rn detector employs a carrier gas, and in order to understand which gas would best perform in a particular experiment, quantitative analyses of different gases are required. In this study, we evaluate the dependence of the calibration factor, which is the proportionality factor between the count rate in the detector and  $^{222}\text{Rn}$  concentration, on absolute humidity of the system, for a  $^{222}\text{Rn}$  detector which employs  $\text{CF}_4$ . This dependence has already been analyzed for Rn detectors that employ purified air, argon (Ar) and Xe gases [17, 18], but not for  $\text{CF}_4$ .

### 2.3 Removal methods

On the other hand, if  $^{222}\text{Rn}$  is to be removed, a quantitative analysis of its adsorption efficiency is needed to accurately predict how much  $^{222}\text{Rn}$  would be removed, and which removal method is valid to use in a particular experiment.

One method of  $^{222}\text{Rn}$  removal is to employ a trap which stores some material with high adsorption, such as activated carbon. Activated carbon has been found efficient at removing  $^{222}\text{Rn}$  from purified air, Ar and Xe gases [19, 20, 21]. It is commonly used in pelletized, granular, powdered, or molded forms. It is charcoal, ingrained with micropores that significantly increase its surface area available for adsorption.

For example, the NEWAGE detector uses an activated carbon trap in the gas circulation line to remove Rn in  $\text{CF}_4$ . It employs 100 g of activated carbon (product name TSURUMICOAL 2GS) to absorb radon and other impurities in a 150 l volume. When the trap is activated, the radon is reduced by 10 times [22], which corresponds to 90% adsorption efficiency. According to an evaluation in Ref. [22], the contribution of  $^{222}\text{Rn}$  to the background of NEWAGE was  $9.3 \text{ mBq/m}^3$ , although recent reports show a value of  $0.5 \pm 0.2 \text{ mBq/m}^3$  from the surface of LA( $\mu$ -PIC) [23].

But a new form – activated carbon fiber (ACF) – was developed in 1966 [24], and commercialized for the use in water purification and surface treatment since the 1990s [18]. In this study, we have used activated an ACF of type A-25, and tested its adsorption properties in Sect. 5, with prospects for its use in experiments, such as NEWAGE.

### 3 An 80 l radon detection system

To accurately detect the amount of  $^{222}\text{Rn}$  in environments for underground experiments, such as Super-Kamiokande, XENON, DRIFT, and NEWAGE experiment, it is customary to use a radon detector. A detection system was developed at Kobe University, which employs the special 80 l radon detector [17], with a PIN photodiode installed for electrostatic collection. Its inner structure is explained in Figure 3.

#### 3.1 Radon detector

In our setup, we employed an  $^{222}\text{Rn}$  detector with a diameter of 500 mm and a volume of 80 l. It has a stainless steel body with ICF (knife-edge) flanges, covered by a metal gasket. In order to reduce the self-contamination background from the detector's surface, electropolishing was carried out during production. The detector surface is grounded. The top part consists of a high voltage divider and an amplifier circuit [25], followed by a ceramic feed-through, which is set to rest on stainless steel plates. The circuit is connected to a 18 mm $\times$ 18 mm PIN photodiode (HAMAMATSU S3204-09), hanging in the top center point of the vessel. This detector uses purified gases; in this study, we used  $\text{CF}_4$  (purity 99.999%).

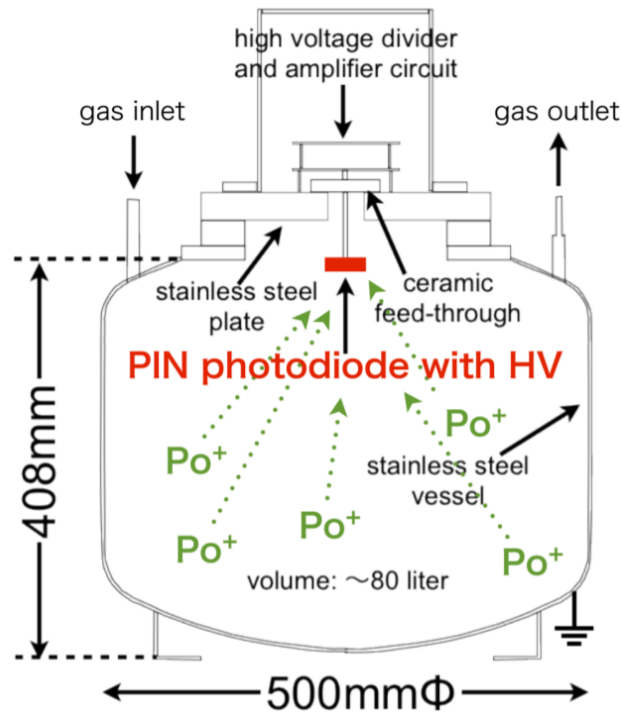


Figure 3: Inner structure of an 80 l radon detector used in this thesis [26].

## 3.2 Detection principle

The carrier gas ( $\text{CF}_4$ ) is let through an inlet on one side and escapes through an outlet on the other. Once the carrier gas is released into the detector,  $^{222}\text{Rn}$  is expected to be mixed with it, and hence some decay patterns start appearing inside the detector, given the intrinsic background of the vessel is lower than the  $^{222}\text{Rn}$  concentration. By applying a reverse bias negative high-voltage to the photodiode and creating an electric field between the photodiode and the vessel, different cations from down the decay chain of  $^{222}\text{Rn}$  start drifting towards the photodiode, and are electrostatically collected and read out at the circuit board in different analog-to-digital converter (ADC) channels. The calibration factor measured in this thesis additionally depends on the high-voltage value of the detector. Previous research suggests  $-2.0$  kV as the optimal value for an 80 l radon detector [27], and so we chose this value for our measurements with  $\text{CF}_4$ .

Two peaks are prominent in the pulse height spectra for this detector. They are visible in Figure 4. These peaks correspond to polonium-218 ( $^{218}\text{Po}$ , 6.11 MeV) and polonium-214 ( $^{214}\text{Po}$ , 7.83 MeV). In this study we used the signal from  $^{214}\text{Po}$  for the integrated count rate, since  $^{214}\text{Po}$  exists at a lower stream of the decay chain, and hence the  $^{222}\text{Rn}$  detector has a higher collection efficiency for  $^{214}\text{Po}$ . In addition to this, while there is a  $^{212}\text{Bi}$  peak (6.21 MeV) close to the  $^{218}\text{Po}$  energy peak, there are no other alpha sources whose energy peaks overlap with the  $^{214}\text{Po}$  peak. The integration range for the count rate was set from 140 to 180 (ADC channels) to maximize  $^{214}\text{Po}$  detection efficiency, similar to how it was done in a previous paper [28]. The settings of the voltage amplifier affect the peak positions. We have checked before each dependence measurement that the peak positions were the same, and therefore the integration range is still appropriate.

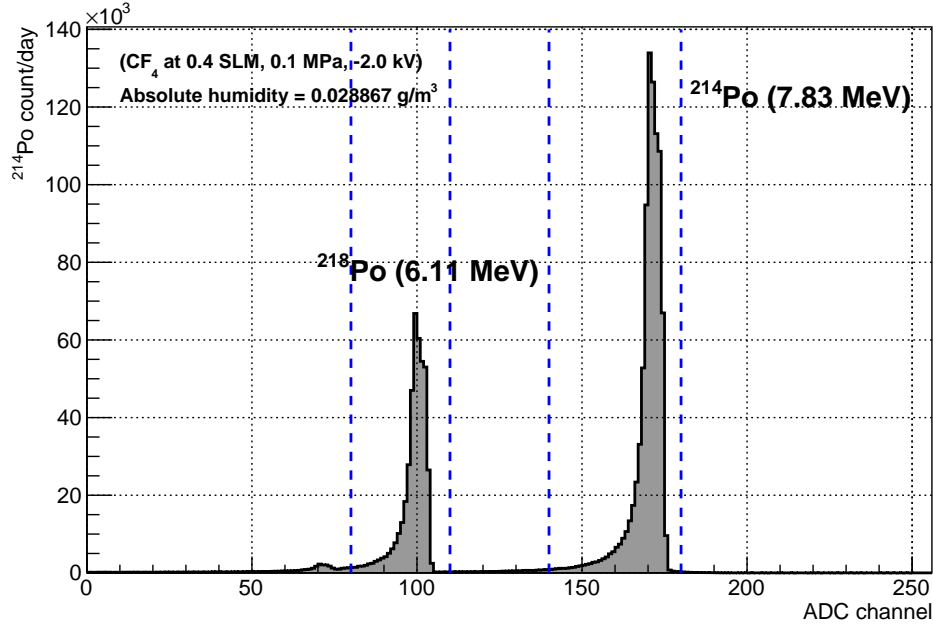


Figure 4: Characteristic pulse height spectrum for  $^{214}\text{Po}$  and  $^{218}\text{Po}$  daily count rates with the integration windows shown in blue vertical lines. Experimental conditions are shown at the top left.

### 3.3 Experimental setup

Previously an 80 l  $^{222}\text{Rn}$  detector has been developed for the use in high-accuracy low-energy experiments: underground particle physics experiments, low-energy dark matter experiments [17, 28, 29]. The detector system we used in this study is one of the calibration systems in Ref. [30], located at Kobe University. This calibration system is shown in Figure 5 and consists of: (1) a  $^{222}\text{Rn}$  source (a Pylon Electronics PYLON RNC  $^{226}\text{Ra}$  container with radioactivity of 78.3 Bq), (2) a mass flow controller (Horiba SEC-Z500X), (3) a refrigerator to control dew point temperature (Iwatani CryoMini PDC08), (4) a cold trap refrigerator (Taisho TC0147), (5) an 80 l  $^{222}\text{Rn}$  detector, (6) a pressure gauge (Swagelok P/N PGU-40-0C30-C-4FSM), (7) a dew point meter (Vaisala DMT152) and (8) a circulation pump (Enomoto Micro Pump Mfg. Co., Ltd. MX-808ST-S). The pressure gauge and the dewpoint meter are connected to the detector.

In Sect. 4, the cold trap refrigerator (4) was bypassed. In both of Rn adsorption efficiency experiments (Sect. 5), we have used 10 g of ACF (A-25, produced by Unitika Ltd.), housed inside the cold trap, its refrigerator connected to the system. The type A-25 was chosen since this type was already tested in a previous study and its properties were evaluated in Xe gas [30].

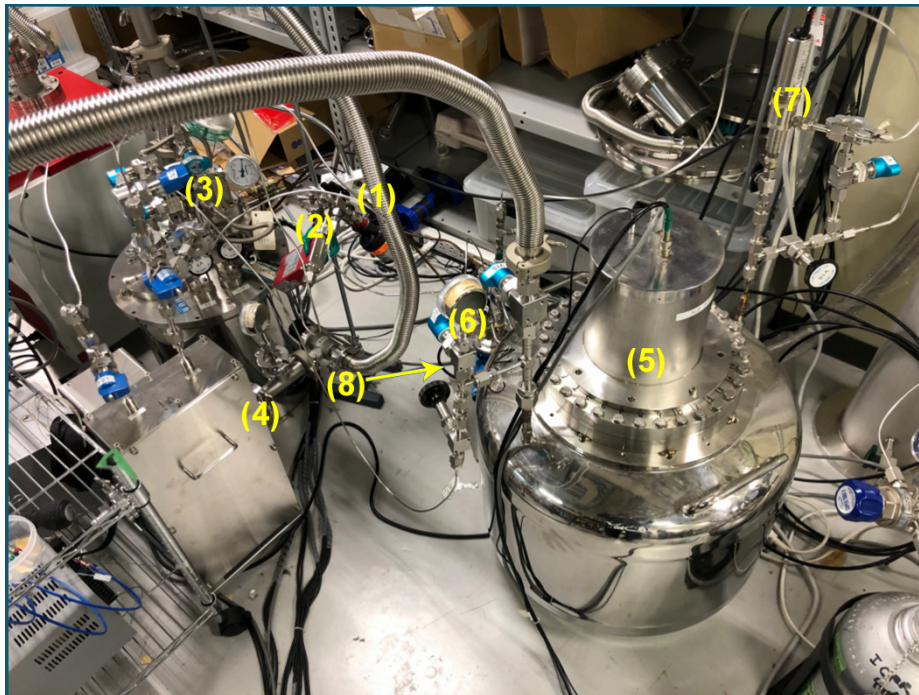
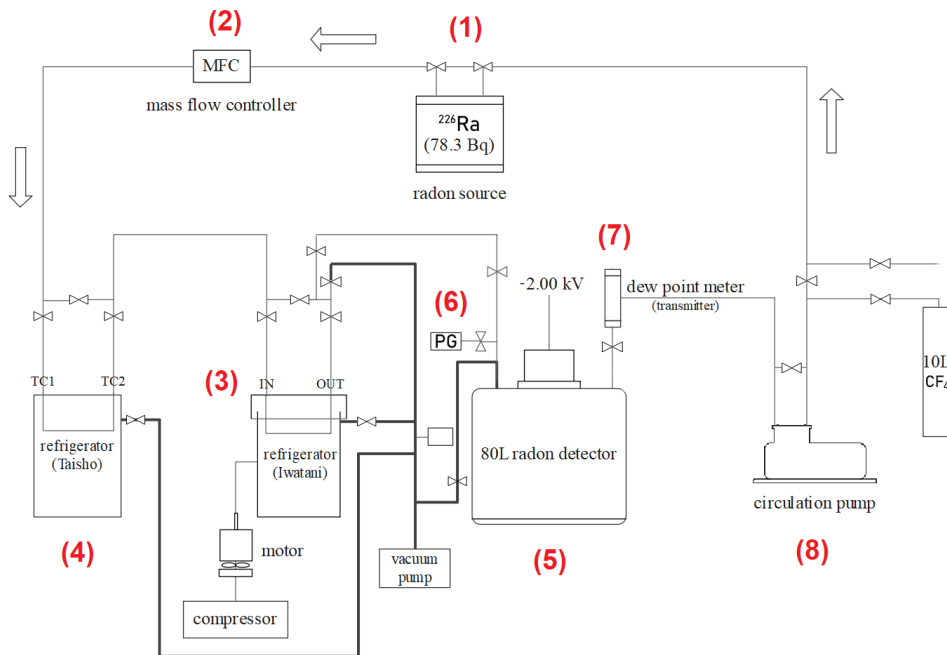


Figure 5: Top: diagram of the detector system at Kobe University. Bottom: photo of the detector system with the corresponding elements numbered (see Sect. 3.3).

# 4 Calibration of the radon detector filled with $\text{CF}_4$

## 4.1 Fundamentals

### 4.1.1 Tetrafluoromethane

Tetrafluoromethane (or  $\text{CF}_4$ ) is a structurally simple chemical compound, which has a low boiling point ( $-127.8^\circ\text{C}$ ). It is sometimes used as a refrigerant and can be prepared by fluorination of carbon dioxide, carbon monoxide or phosgene with sulfur tetrafluoride. Of particular interest, however, is its remarkable bond strength, owing to fluorine's high electronegativity and multiple carbon-fluorine bonds, which are the strongest in organic chemistry [31]. This property lends them to be a good quenching gas choice in neutron detectors [32], target material for neutrino detection [33], and a carrier gas in dark matter search experiments, such as the NEWAGE experiment [12] or the DRIFT experiment [34]. In particular,  $\text{CF}_4$  is the target in the NEWAGE experiment since its fluorine nuclei have a large scattering cross-section for spin-dependent WIMP-nucleus interactions in extensions of the Standard Model of particle physics with WIMPs [35].

In view of  $\text{CF}_4$  potential use in low-energy underground experiments, it was employed in this study in an 80 l radon detection system. As described in the next chapters, we tested the adsorption properties of a novel adsorption material called activated carbon fiber inside of  $\text{CF}_4$  gas.

### 4.1.2 Calibration factor

The calibration factor of a radon detector is the proportionality factor between the ADC count of the  $^{214}\text{Po}$  ions inside the detector and  $^{222}\text{Rn}$  concentration. Knowing the value of this factor is crucial for properly maintaining low background levels in low-energy experiments. In this section, we measure the calibration factor of this detector and analyze its absolute humidity and  $^{222}\text{Rn}$  concentration dependence. This kind of quantitative analysis has not been yet done for  $\text{CF}_4$  gas.

The calibration factor ( $C_F$ ) was calculated the following way:

$$C_F [(\text{count/day})(\text{Bq}/\text{m}^3)] = \frac{\text{ADC count} [\text{count}/\text{day}]}{\text{expected } ^{222}\text{Rn concentration} [\text{mBq}/\text{m}^3]}, \quad (1)$$

where ADC count is measured by the Rn detector and the expected  $^{222}\text{Rn}$  concentration is calculated from the activity of the Rn source and the volume of the calibration system:  $^{222}\text{Rn}$  concentration =  $78.3 \text{ Bq}/0.08 \text{ m}^3 = 978.7 \text{ Bq}/\text{m}^3$  under radioactive equilibrium.

### 4.1.3 Neutralization rate

In a radon detector,  $^{214}\text{Po}$  ions, created in the alpha decay of  $^{222}\text{Rn}$ , pass through the gas while drifting to the photodiode, and while doing so, have a small probability to scatter

off water molecules and become neutralized. When the ions are neutralized, they are not electrostatically collected at the photodiode surface, and their count rate drops. The rate at which this scattering occurs is called the neutralization rate (for a certain carrier gas). For daughter particles of  $^{222}\text{Rn}$ , neutralization rate was first researched in 1988 for the case of  $^{218}\text{Po}$  [36]. Since  $^{214}\text{Po}$  ions are isotopes of  $^{218}\text{Po}$  and are also daughter particles of  $^{222}\text{Rn}$  slightly further down the chain, the analysis for neutralization rate should apply in a similar manner.

The decrease in the rate of Po ions collected electrostatically should be accounted for in the calibration factor. Phenomenological analysis predicts that this decrease comes mainly from the neutralization rate, which, for small ions, is proportional to the square root of absolute humidity of the gas [36]. In a similar way, in Ref. [28], calibration factor has been found to be best described by a negative square root dependence on absolute humidity for other gases (air, Ar and Xe).

To calculate absolute humidity in the carrier gas, we first need to know the saturated vapor pressure of ice,  $P$  [kPa] which is given by the following formula [37]:

$$P = \exp\left(-\frac{6024.5282}{T_{dew}} + 29.3271 + 0.0106139 T_{dew} + 0.0000132 T_{dew}^2 - 0.4938258 \ln T_{dew}\right) \quad (2)$$

Here, the dew point temperature ( $T_{dew}$ ) is in units of kelvin.

The formula for absolute humidity ( $AH$  [ $\text{g}/\text{m}^3$ ]) is a simple relation between  $P$  and the air temperature ( $T_{air}$  [ $^{\circ}\text{C}$ ]) in the carrier gas:

$$AH = \frac{0.00794 P}{1 + 0.00366 T_{air}}. \quad (3)$$

#### 4.1.4 Absolute humidity

For our analysis of calibration factor's dependence on absolute humidity we used the system described in Sect. 3.3, but with only one refrigerator to control the dew point temperature (the cold trap refrigerator was bypassed). By specifying a setpoint temperature, the refrigerator will stabilize the system to a dew point temperature of approximately the same value within 20 hours on average. From there, we can calculate the absolute humidity for a known dew point.

## 4.2 Absolute humidity dependence

Before starting the measurements, the inside of the detector was sufficiently vacuumed with the use of the turbomolecular vacuum pump, shown in Figure 5 (top). In our study, the flow rate was set to 0.4 standard liter per minute (SLM) using the mass flow controller. Next,  $\text{CF}_4$  was introduced into the system. The refrigerator was turned on, its setpoint was set to  $-30^{\circ}\text{C}$ , and the dew point temperature allowed half a day to stabilize. A period where the dew point temperature is approximately constant was selected, and the average value of  $^{214}\text{Po}$  count rate was calculated for that period in order to determine

the calibration factor. It was then converted to the calibration factor using Eq. (1). In our analysis of humidity dependence, we used a constant  $^{222}\text{Rn}$  concentration (under radioactive equilibrium), calculated from the radioactivity of the source and detector volume. This procedure was performed for eight setpoint values, for which nine periods in total were selected (two periods were selected for setpoint at  $-50^\circ\text{C}$ ). The last data range was obtained with the refrigerator turned off (room temperature was  $+25^\circ\text{C}$ , corresponding to a dew point in  $\text{CF}_4$  of  $-11^\circ\text{C}$ ). The time variation of the  $^{214}\text{Po}$  count rate (per hour) and the dew point temperature are shown in Figure 6. We have additionally calculated the calibration factor for a short period before the refrigerator was turned on (days 0.44–0.71). However, this period is too short for an accurate average  $^{214}\text{Po}$  count value, since there is a possibility of  $^{214}\text{Po}$  count being unstable, and thus we calculated the conversion factor using the data taken during this period, while we excluded this data from the absolute humidity dependence. Table 1 shows the data ranges and experimental variables for those ranges. A close-up graph of one of the fitting regions is given in Figure 7.

Time period [d]	$^{214}\text{Po}$ count [/day]	Calibration factor [(count/day)/(mBq/m <sup>3</sup> )]	Absolute humidity [g/m <sup>3</sup> ]
0.44 – 0.71†	$324118 \pm 55$	$0.331 \pm 0.038$	1.17480
1.9 – 2.1	$795352 \pm 166$	$0.813 \pm 0.094$	0.06118
6.0 – 6.6	$875040 \pm 101$	$0.894 \pm 0.103$	0.02887
16.0 – 16.77	$832938 \pm 87$	$0.851 \pm 0.098$	0.01415
18.67 – 19.90	$852914 \pm 69$	$0.871 \pm 0.100$	0.01437
20.90 – 21.10	$866582 \pm 173$	$0.885 \pm 0.102$	0.00594
22.96 – 23.67	$837038 \pm 90$	$0.855 \pm 0.099$	0.00172
29.0 – 31.48	$842797 \pm 49$	$0.861 \pm 0.099$	0.00035
33.17 – 33.88	$844224 \pm 91$	$0.863 \pm 0.099$	0.00003
73.0 – 74.0	$314667 \pm 47$	$0.321 \pm 0.037$	1.75331

Table 1: Data ranges and values of experimental variables used in calculating the calibration factor of a  $^{222}\text{Rn}$  detector with  $\text{CF}_4$ . The data range with † was not included in the final calculation.

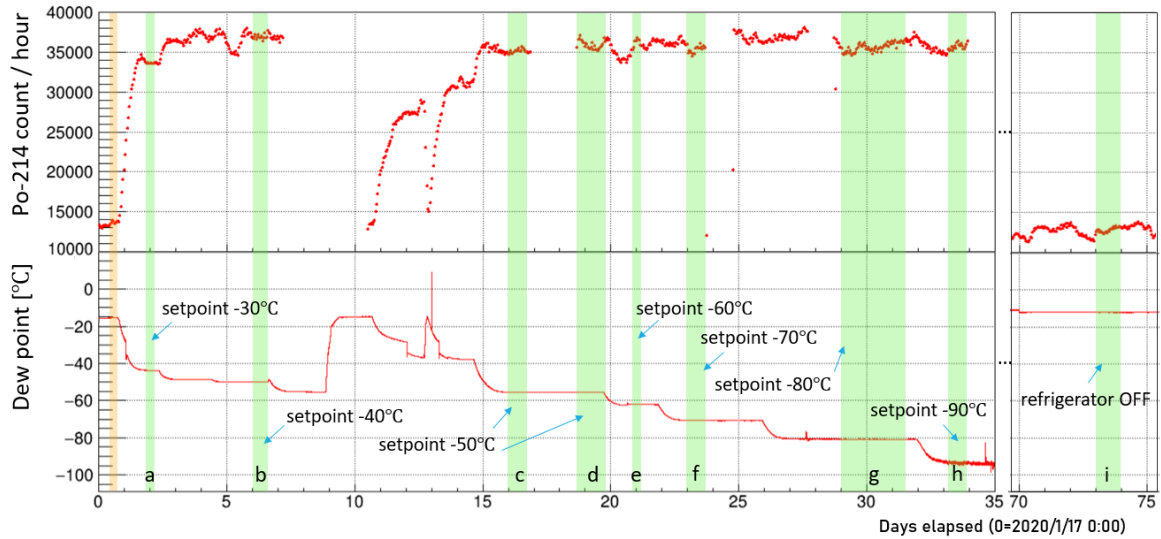
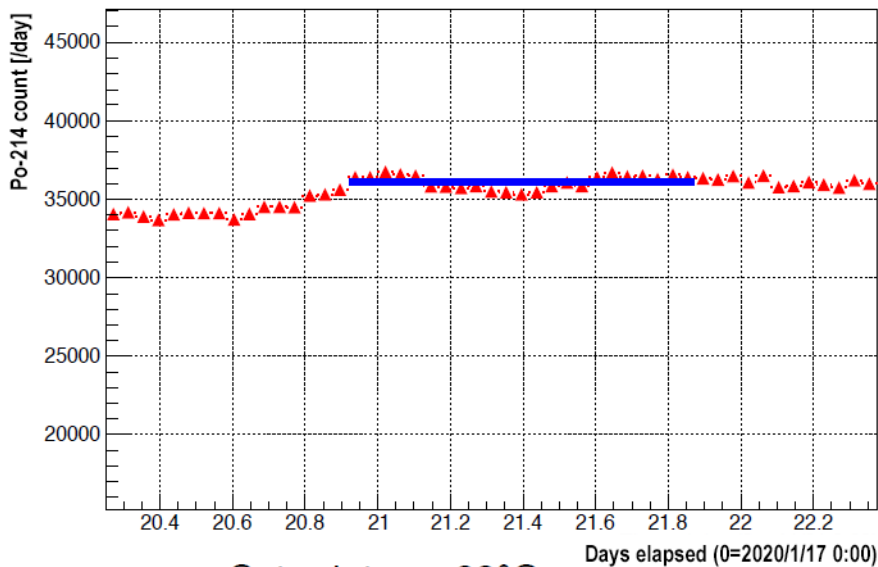


Figure 6: Time variation of the  $^{214}\text{Po}$  count rate and the dew point temperature in the detector filled with  $\text{CF}_4$ , along with the nine analyzed data ranges (shown in green, marked by letters from a to i, corresponding to setpoint values from  $-90^\circ\text{C}$  to room temperature). The range shown in orange is the short period before the refrigerator was turned on that was additionally analyzed.

e



Setpoint:  $-60^\circ\text{C}$   
 Day Range: 20.92~21.88  
 Dewpoint:  $-62.12^\circ\text{C}$   
 Count/1h: 36111.5

Figure 7:  $^{214}\text{Po}$  count rate in the data range e, along with the parameters for the constant fit below.

Figure 8 shows the resulting calibration factor as a function of absolute humidity for the case of  $\text{CF}_4$ , along with the results for other gases [17, 28]. The fitted function for the case of  $\text{CF}_4$  is given by:

$$C_F = -0.44\sqrt{AH} + 0.90, \quad (4)$$

where  $AH$  is the absolute humidity in the gas ( $\text{g}/\text{m}^3$ ). This demonstrates that the calibration factor of  $\text{CF}_4$  gas clearly depends on its humidity with a negative square root functional form similar to other gases. The calibration factor has a flat region for  $AH$  below  $10^{-2} \text{ g}/\text{m}^3$ , but drops to half its value at  $AH$  around  $1 \text{ g}/\text{m}^3$ . This calibration factor, however, is lower at dry humidities than for any other gas measured so far. We suggest the reason for this in Sect. 6.1, where we analyze the  $\sigma$  parameter of the Lennard-Jones potential of different carrier gases.

Below are some typical values of the calibration factor (data regions h (setpoint at  $-90^\circ\text{C}$ ) and i (refrigerator off) in Figure 6) at specified absolute humidities, with systematic uncertainties included (described below):

$$C_F \text{ (region h)} = 0.87 \pm 0.04 \text{ (count/day)/(\text{mBq}/\text{m}^3) \text{ at } 3 \times 10^{-5} \text{ g}/\text{m}^3,$$

$$C_F \text{ (region i)} = 0.33 \pm 0.02 \text{ (count/day)/(\text{mBq}/\text{m}^3) \text{ at } 1.75 \text{ g}/\text{m}^3.$$

For the calibration factor measurements, the systematic uncertainties were estimated along the same way as in Ref. [17]. The uncertainties come from: accuracy of radioactivity of the  $^{222}\text{Rn}$  source —  $\pm 4.0\%$ , accuracy of the dewpoint meter —  $\pm 2.0\%$ , and accuracy of the estimation of the total volume of the calibration system, including the 80 l detector and vacuum tubing —  $\pm 2.0\%$ . All of the accounted uncertainties are presented in Table 2.

Cause†	Uncertainty [%]
Accuracy of radioactivity of the $^{222}\text{Rn}$ source†	$\pm 4.0$
Accuracy of the dewpoint meter†	$\pm 2.0$
Accuracy of the total volume estimation of the calibration system	$\pm 2.0$

Table 2: Systematic uncertainties on the calibration factor of a  $^{222}\text{Rn}$  detector with  $\text{CF}_4$ . Uncertainties marked with † come from the technical specifications of the measurement devices.

Lastly, we have considered a different integration range for the count rate of  $^{218}\text{Po}$ , with ADC channels 120 to 180. Using this range, we calculated the calibration factor for the same dataset, obtaining:

$$C_F = -0.44\sqrt{AH} + 0.91, \quad (5)$$

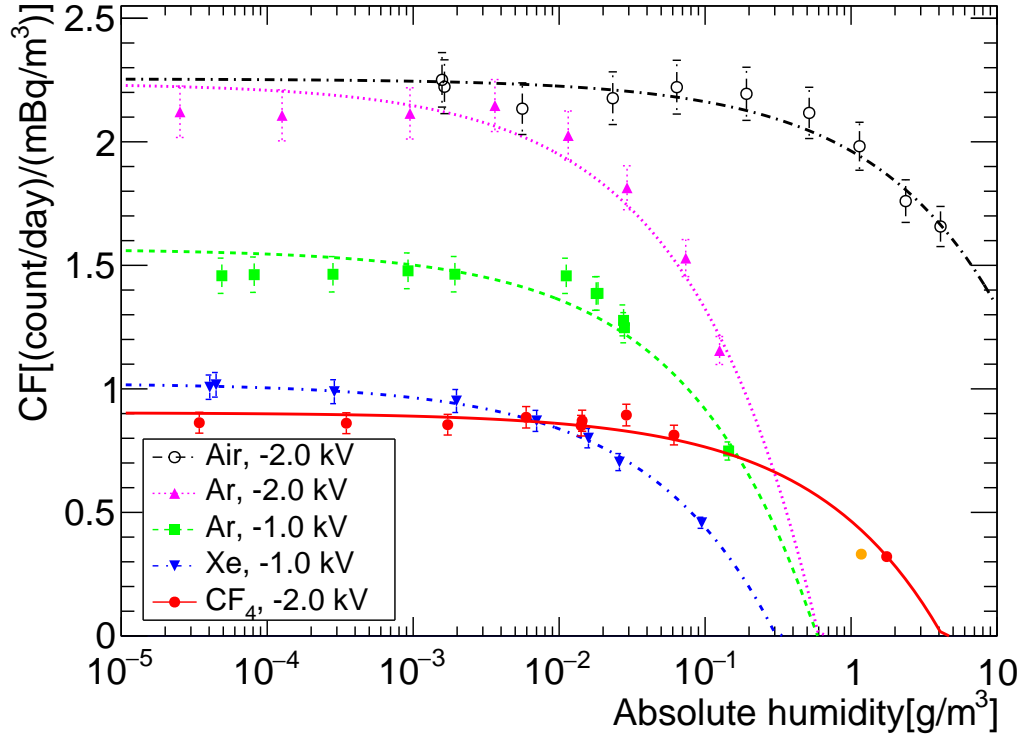


Figure 8: Calibration factor of the 80 l  $^{222}\text{Rn}$  detector as a function of absolute humidity for  $\text{CF}_4$  and other gases: purified air (black) [28], Ar (pink and green), Xe (blue) and  $\text{CF}_4$  (red) [17]. The vertical error bars for  $\text{CF}_4$  include statistical and systematic errors described in Table 2. One point drawn in orange is the calibration factor calculated from the short period before the refrigerator was turned on.

which is almost identical to the above function for  $C_F$  for ADC channels 140 to 180. Although there is a slight overlap with signals from daughter particles in the thorium decay chain in ADC channels around 130, the test was useful to show that a change in the integration range does not influence the calibration factor value considerably.

### 4.3 Radon concentration dependence

To evaluate the dependence of the calibration factor on  $^{222}\text{Rn}$  concentration, we bypassed the  $^{222}\text{Rn}$  source and allowed the  $^{222}\text{Rn}$  in the system to decay to the background level. The gas flow was still maintained with the circulation pump at 0.4 SLM. The refrigerator was off, the dew point stable at around  $-11^\circ\text{C}$ .

Its decay part was then fitted with a free half-life parameter (red line in Figure 9) using the formula:  $p_0 \cdot 2^{-\frac{x-t_0}{p_1}} + p_2$ , where  $p_0$ ,  $p_1$ ,  $p_2$  are the parameters to be fitted,  $t_0$  is the starting time of the decay. The half-life parameter was equal to  $3.99 \pm 0.01(\text{stat.})$  days. This differed from the usual value of 3.82 days, suggesting us to calculate the expected concentration (obtained from the fit with the half-life parameter = 3.82 days

and a constant calibration factor) and the raw concentration (from the free fit) and plotted their ratio against the expected concentration. This ratio is shown in Figure 10. It was also fitted with a piecewise function, shown in red. For concentration ratios above 1.3, a constant fitting function was chosen; for ratios below 1.3, the function was exponential. Furthermore, concentrations above  $978.7 \text{ Bq/m}^3$ , which is the expected concentration, calculated from the activity of the  $^{222}\text{Rn}$  source in Sect. 4.1.2, are not shown. It is clear that the ratio of the expected concentration versus the raw concentration exceeds 1, which is unphysical, and requires a systematic error. From this analysis, although the exact reason is unknown, it was confirmed that the detection efficiency differs by about  $\pm 17\%$  at different  $^{222}\text{Rn}$  concentrations between several  $\text{mBq/m}^3$  and  $10^6 \text{ mBq/m}^3$ .

After multiplying the calibration factor by the fitted ratio function, which serves as the concentration dependence correction factor, we calculated the  $^{222}\text{Rn}$  concentration again and fitted the corresponding decay. This time, the half-life parameter was found to equal  $3.80 \pm 0.01$  days, which is more consistent with the expected value for a pure decay of  $^{222}\text{Rn}$ . This gives some insight into how the calibration factor of a  $^{222}\text{Rn}$  detector could potentially depend on the amount of  $^{222}\text{Rn}$  in the system and requires further investigation.

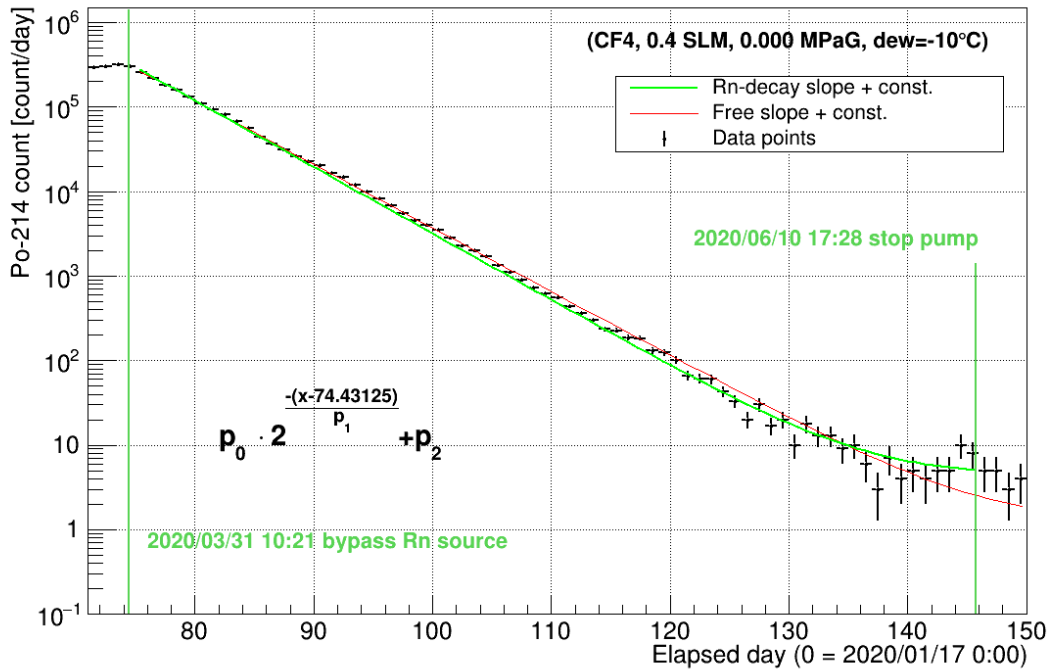


Figure 9: Time variation of the  $^{214}\text{Po}$  count rate during the measurement of concentration dependence. The formula on the left shows the fitting function for the free slope. The experimental conditions are written at the top right.

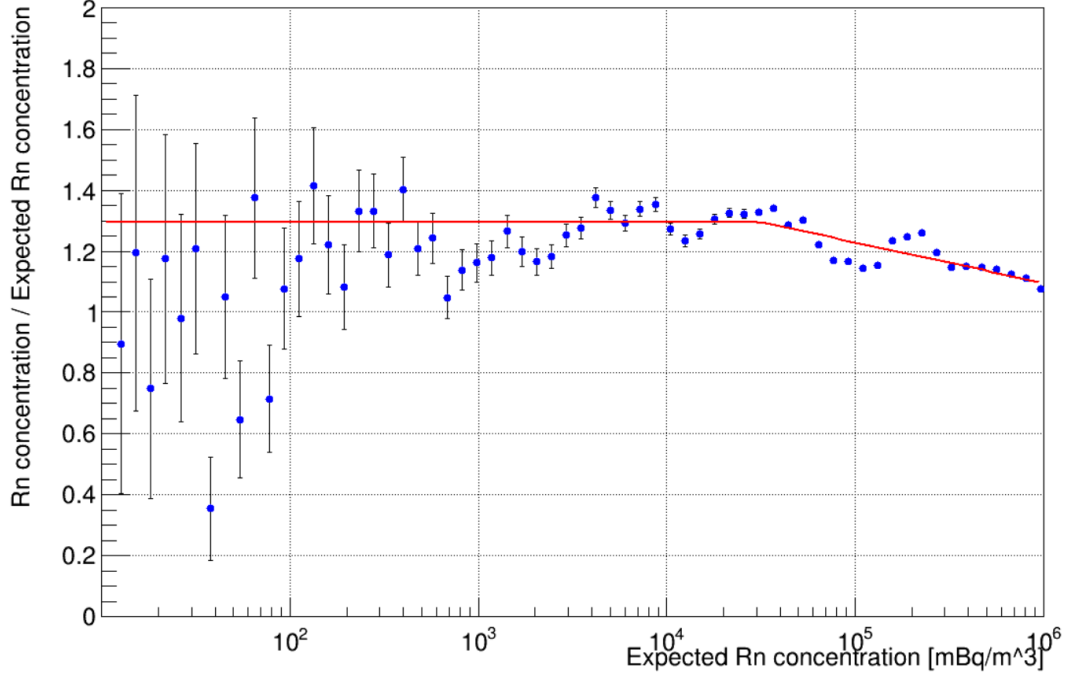


Figure 10: Ratio of raw concentration (obtained from the free fit) to expected concentration (obtained from the fit with the half-life parameter = 3.82 days and a constant calibration factor). Its fit is shown in red. The maximum (cutoff) value is  $978.7 \text{ Bq/m}^3$  (Sect. 4.1.2).

## 4.4 Background run

Lastly, we have measured the background level of the system. After the decay part, described in the previous section, the  $^{214}\text{Po}$  count reached a constant rate. We measured it for 14.5 days and obtained an average rate of  $1.24 \pm 0.09$  (stat. only) count/day for the system background. The pulse height spectrum for this period is shown in Figure 11.

We found some alpha sources originated from the thorium decay series, such as  $^{224}\text{Ra}$ ,  $^{212}\text{Bi}$ ,  $^{220}\text{Rn}$ ,  $^{216}\text{Po}$ ,  $^{212}\text{Po}$ . Their spectra do not overlap with the  $^{214}\text{Po}$  signal region. Thus, the background measurement was appropriately performed without contamination from other alpha sources. Since this measurement was performed at the end of a 170-day long decay of  $^{222}\text{Rn}$ , the count rate of  $^{210}\text{Po}$  in the background spectrum is high in comparison with other alpha sources. The increase is likely due to positively charged  $^{210}\text{Pb}$  from the  $^{222}\text{Rn}$  decay chain accumulating on the surface of the PIN photodiode over the measurement history of the detector. Since it decays with a half-life of 22 years to produce the observed  $^{210}\text{Po}$ , the increased count rate indicates that  $^{222}\text{Rn}$  daughters remain on the photodiode once they have been collected.

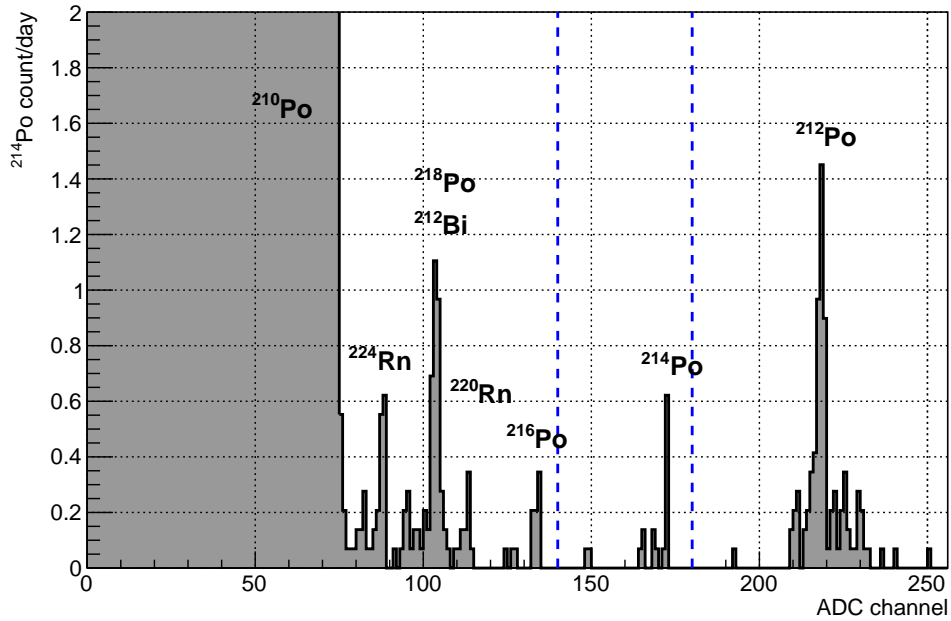


Figure 11: The pulse height spectrum for the 14.5-day measurement of the background of a  $^{222}\text{Rn}$  detector filled with  $\text{CF}_4$ .  $^{224}\text{Ra}$  (5.79 MeV),  $^{212}\text{Bi}$  (6.21 MeV),  $^{220}\text{Rn}$  (6.40 MeV),  $^{216}\text{Po}$  (6.91 MeV) and  $^{212}\text{Po}$  (8.78 MeV) originate from the thorium decay series. Those come from the inner surface material of the Rn detector and result in the intrinsic background of the Rn detector. The integration window of  $^{214}\text{Po}$  is shown in blue vertical lines.

Comparing this measurement to previous measurements done on the same detector [17], where the background level was  $0.81 \pm 0.08(\text{stat. only})$  [count/day] for purified air ( $-2.0$  kV), the background level of  $\text{CF}_4$  ( $-2.0$  kV) is about 1.5 times as prominent. While the current measurement was done on the whole system, as opposed to previous measurements on the 80 l detector, the value is nonetheless acceptable and low enough to have negligible effects on measurements in this study.

# 5 Measurement of radon adsorption efficiency of ACF

To evaluate the  $^{222}\text{Rn}$  adsorption efficiency of an ACF, we used the setup described in Sect. 3.3, with the trapped refrigerator bypassed at first. The other refrigerator (Iwatani) is set to  $-60^\circ\text{C}$  to maintain a low dew point throughout the experiment. Hence, in this experiment, we have tried to eliminate dependence on absolute humidity. We have used the calibration factor found previously to calculate the  $^{222}\text{Rn}$  concentration henceforth.

We carried out two experiments: an adsorption test at atmospheric pressure and a pressure dependence experiment, with multiple adsorption tests at different pressure levels, while the Rn source was bypassed.

## 5.1 Activated carbon fiber

ACF is a powerful adsorbent due to its large surface area and low intraparticle diffusion, and hence, smaller and flexible size of its units in practice. However, ACF's application to removing  $^{222}\text{Rn}$  in purified gases has not been explored, except for the case of  $^{222}\text{Rn}$  in purified air, Ar and Xe gases [30, 38]. In this thesis, we aim to evaluate the Rn adsorption efficiency of ACF in  $\text{CF}_4$ .

The surface of an ACF contains numerous micropores, with a typical size of several nanometers (Figure 12). These micropores are all comparable in size, which allows for faster adsorption times for homogeneous mixtures. Compared to pellet and granular adsorbents, adsorbates in ACF are not subjected to the diffusion resistance of macropores, hence it is easy and efficient to employ in a variety of mixtures [24]. When a free particle gets close to the entrance of a micropore, a potential difference is induced due to the attraction term ( $r^{-6}$ ) of the Lennard-Jones potential, and the particle is adsorbed at the surface of the pore, due to the van der Waals forces. Since this term is sharp, the size of the adsorbed particle must be close to the pore size for this attraction to prevail, hence the nanometer pore size.

Recent evaluations using different ACF types (products of Unitika Ltd.): pore diameters 1.7—5.3 nm, specific surface areas 850—2667  $\text{m}^2/\text{g}$ , showed good adsorption in Xe gas, especially using ACF types A-20 and A-25 [30]. In this study, we have used an ACF of type A-25, with a specific surface area of 2667  $\text{m}^2/\text{g}$  and pore diameter 2.5 nm.

A good estimator of a Rn trap's performance is the Henry's constant. Henry's constant is the constant in Henry's law of gases. Good comparisons of Henry's constant, specifically the two-component gas version [21], among different adsorbents are done in Ref. [21] and Ref. [30]. Table 3 shows the summary of Henry's constants of the adsorbents in Xe gas. The Henry's constant value for type A-25 ACF exceeds previous results. This shows that ACF is an efficient adsorbent, and has led us to choose A-25 as the ACF in this experiment.

Adsorbent [MPa]	Xe pressure [MPa]	Temperature [°C]	$\tilde{H}$ [ $10^{-4}$ mol/(Pa · kg)]
Roth MS5Å	0.0255	21	$1.32 \pm 0.03$
Roth MS10Å	0.0255	21	$1.31 \pm 0.03$
SHIRASAGI G <sub>2x</sub> 4/6	0.0255	21	$3.9 \pm 0.2$
Cu <sub>3</sub> (BTC) <sub>2</sub> MOF	0.0255	21	$2.03 \pm 0.07$
Blücher 100878	0.0255	21	$4.4 \pm 0.2$
Blücher 100050	0.0255	21	$3.5 \pm 0.2$
Blücher 100050	0.020	-40	$6.7 \pm 0.5$
Blücher 100050	0.020	-71.1	$19.4 \pm 2.4$
Unitika ACF A-25	0.029	-95	$50 \pm 10$

Table 3: Henry’s constants of different typical adsorbents in Xe gas. Here, “SHIRASAGI G<sub>2x</sub> 4/6”, “Blücher 100878” and “Blücher 100050” are activated carbons, and “Unitika ACF A-25” is ACF. Data taken from Ref. [21] and Ref. [30].

## 5.2 Cold trap

Figure 13 (left) shows the inner structure of the cold trap. It features a U-shaped tube, where the ACF is housed, and which leads the gas from the inlet (A) to the outlet (B). When the trap’s refrigerator, set to a low temperature, is connected ( $t_0$  in Figure 13 (right)), <sup>222</sup>Rn, present in the carrier gas, gets slowed down significantly and retains inside of the trap material for a certain period of time. During this period, the <sup>222</sup>Rn concentration drops to a minimum and some of the <sup>222</sup>Rn gets adsorbed ( $t_1$  to  $t_2$ ). After this, <sup>222</sup>Rn that did not get adsorbed exits the trap into recirculation, and we see a corresponding increase in <sup>222</sup>Rn concentration ( $t_2$  to  $t_3$ ). While <sup>222</sup>Rn is in the trap, it undergoes both turbulent behavior and longitudinal diffusion along the length of the trap, which causes gradual damping of the oscillation pattern in concentration ( $t_3$  to  $t_n$ ). The time in which the <sup>222</sup>Rn concentration becomes stable varies with the flow rate in the system. In this study, all measurements were performed at 0.4 standard liter per minute (SLM). The stabilization time for these conditions was found to be around 7 days.

## 5.3 Radon adsorption efficiency at atmospheric pressure

In this experiment, CF<sub>4</sub> gas was already circulating in the system. The initial temperature was the room temperature (+25°C). We call this the “bypass phase”, since the cold trap refrigerator was bypassed. After the flow rate was fixed at 0.4 SLM, the cold trap refrigerator was set to a temperature of −95°C and connected to the system, initiating the “adsorption phase”. The measurements were carried out for 19.5 days before the

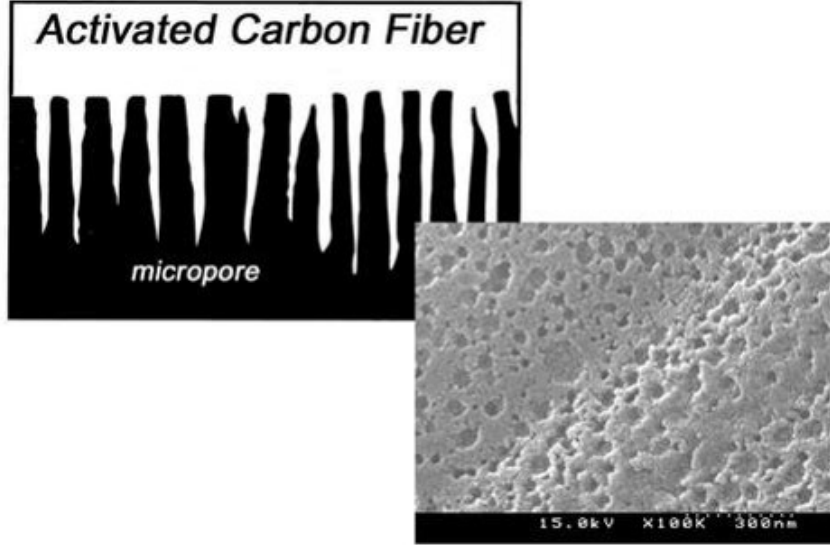


Figure 12: Microporous structure of a typical ACF: a drawing of a cross-section (top), and a top-view microscope image (bottom) [39].

refrigerator was turned off. Thus began the “off phase”. In the “off phase”, we collected data for a couple more days. Even though the refrigerator was turned off, the trap was still operational, and hence some of the original Rn was still trapped inside, lowering the  $^{222}\text{Rn}$  concentration for this region. The  $^{222}\text{Rn}$  concentration variation during the experiment is shown in Figure 14. It was calculated from the integrated count rate for  $^{214}\text{Po}$  using the calibration factor function found in Sect. 4.2. We have also observed a pressure drop of about 0.01 MPa in the adsorption phase.

The oscillatory pattern of the Rn concentration measured with the Rn detector is thought to correspond to the characteristic  $^{222}\text{Rn}$  adsorption behavior of the trap. This behavior is damped by the turbulence and longitudinal diffusion along the length of the trap [19]. Note that there was still some turbulence after the oscillation had dampened out, which is the random turbulence due to the stochastic nature of the cold trap.

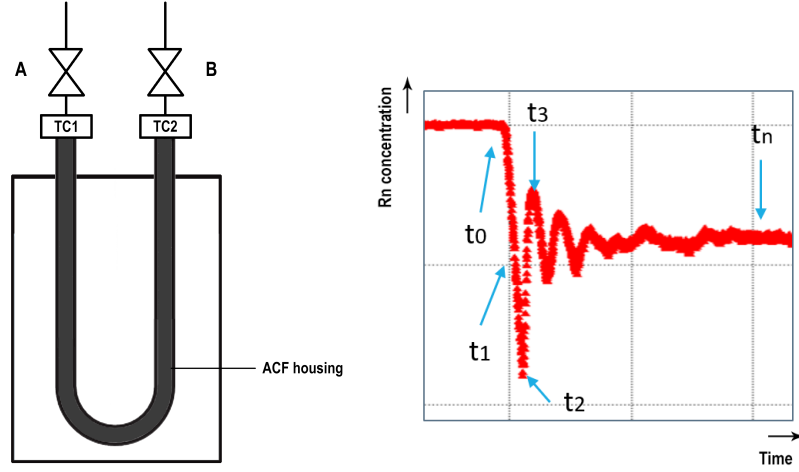


Figure 13: Left: inner structure of the cold trap. Right: temporal evolution of  $^{222}\text{Rn}$  concentration with the cold trap's refrigerator turned on at  $t_0$  (more in Sect. 5.2). This is a picture of the oscillation in Sect. 5.3.

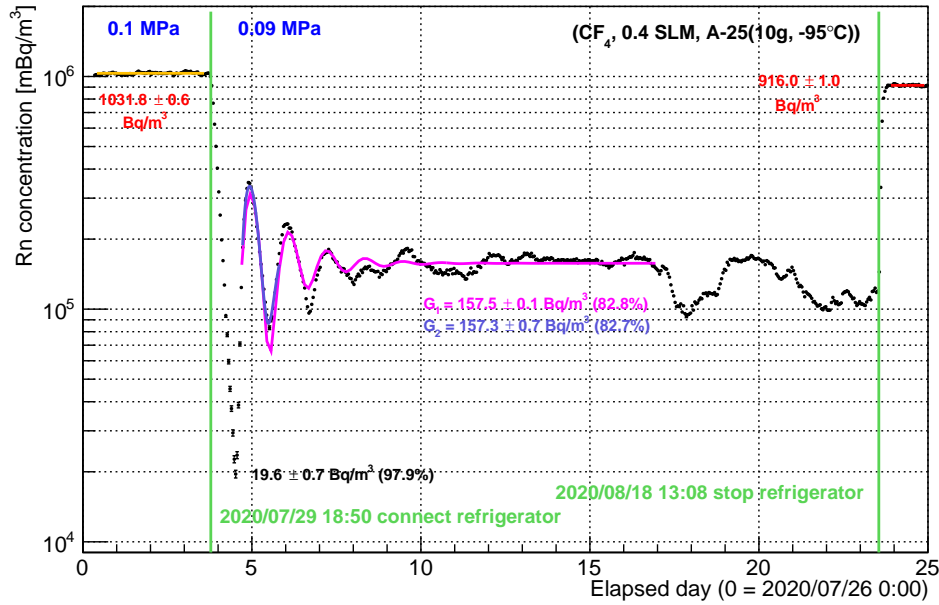


Figure 14:  $^{222}\text{Rn}$  concentration variation in  $\text{CF}_4$  in the  $\text{Rn}$  adsorption efficiency experiment. Orange and red lines show fitting results during the bypass and off phases, respectively. The fitting functions for methods (1) and (2) are shown in magenta and blue lines, respectively.  $G_1$  and  $G_2$  are the values of the fitting parameters  $G$  in methods (1) and (2). The experimental conditions are shown at the top.

We calculate the adsorption efficiency ( $E_{\text{ads}}$ ) by comparing the  $^{222}\text{Rn}$  concentrations in the off phase (at  $+25^\circ\text{C}$ ) and in the adsorption phase (at  $-95^\circ\text{C}$ ):

$$E_{\text{ads}} = \frac{C_{\text{off}} - C_{\text{adsorbed}}}{C_{\text{off}}} \times 100.0 \text{ [\%]}, \quad (6)$$

where  $C_{\text{off}}$  ( $C_{\text{adsorbed}}$ ) is the Rn concentration in the off (adsorption) phase.

For the concentration in the adsorption phase, we have evaluated it by fitting with a damped sinusoidal function of the form  $f(t) = A \cdot e^{-Bt} \sin(Dt + F) + G$  in the region of interest: starting after the first oscillation minimum and including the oscillation and the whole stable region after it. Since the asymptote for the function  $f(t)$  is  $G$ , we used the value of  $G$  as  $C_{\text{adsorbed}}$  in method (1) in Table 4. We then performed another fit with free parameters for the same function  $f(t)$ , this time in a region between two datapoints with approximately the same  $^{222}\text{Rn}$  concentration value, but separated by at least 1 period of oscillation. For this, we chose the region between the first maximum and the second minimum of oscillation. We found a similar value of  $G$ , which is used in method (2) in Table 4.

Having a fitting region with a length close to 1 full period allows us to maximize the fitting accuracy from the sinusoidal part of the function, in the case that the actual Rn concentration function has additional functional dependencies, different from our chosen fitting function,  $f(t) = A \cdot e^{-Bt} \sin(Dt + F) + G$ . The systematic uncertainty associated with this choice of a fitting method is estimated later.

The difference between concentration (and hence – adsorption efficiency) values in methods (1) and (2) is sufficiently small to allow us to choose method (2) as the main method. Even though method (2) has a larger uncertainty, it is crucial for evaluations in Sect. 5.4, where the time until  $^{222}\text{Rn}$  decays fully was limited, and it was not possible to wait the whole stabilization period of 7 days multiple times to collect stable data in the adsorption phase.

Evaluation method	$^{222}\text{Rn}$ concentration [Bq/m <sup>3</sup> ]	Adsorption efficiency [%]
Method (1): long fitting region	$157.5 \pm 0.1(\text{stat.})$	$82.8 \pm 0.1(\text{stat.}) \pm 2.2(\text{syst.})$
Method (2): short fitting region	$158.3 \pm 0.7(\text{stat.})$	$82.7 \pm 0.1(\text{stat.}) \pm 2.3(\text{syst.})$

Table 4: Comparison of evaluation methods for  $^{222}\text{Rn}$  adsorption efficiency in  $\text{CF}_4$ . The systematic errors are obtained from Table 7.

We have also calculated the efficiency at the oscillation minimum. This point indeed corresponds to maximum adsorption efficiency:  $E_{\text{ads}}(\text{osc. min.}) = 97.9 \pm 0.1(\text{stat.})\%$ .

## 5.4 Pressure dependence of radon adsorption efficiency

Next, we have conducted an experiment to evaluate the pressure dependence of an ACF's Rn adsorption efficiency. In a lot of dark matter search experiments (such as NEWAGE) it is necessary to operate with gases at low pressures. Therefore, in this experiment, we have tested whether the Rn adsorption efficiency is sufficient at low pressures. The pressure levels were chosen to go from 0.10 MPa in steps of 0.02 MPa, with the exception of the last level, which, due to the limitations of the circulation pump, was set as 0.03 MPa.

Since this experiment is continued from the experiment at atmospheric pressure (Sect. 5.3),  $\text{CF}_4$  is already introduced in the system and the trap is turned on. Before the measurement procedures, the cold trap refrigerator was baked at  $+85^\circ\text{C}$  and the inside of the detector was sufficiently vacuumed with the use of the turbomolecular pump. After baking, we lowered the temperature to room temperature. Since the Rn source employed cannot be used at low pressures, according to the specifications, it was then bypassed from the system, and data taking began. Shortly after that, we used the turbomolecular pump to lower the pressure level down to 0.08 MPa. After we left the system for some time, sufficient for fitting, we turned on the refrigerator, which brought the temperature down to  $-95^\circ\text{C}$ . This has accelerated the adsorption process so that the characteristic oscillation pattern appeared in the  $^{222}\text{Rn}$  concentration, as shown in Figure 15. Continuing the method from Sect. 5.3, in the activated (adsorption) region it was sufficient for us to collect data until about the second maximum. Finally, we turned the refrigerator off and allowed roughly the same amount of time to obtain data for fitting. These procedures were then repeated at 0.06 MPa, 0.04 MPa and 0.03 MPa. They are summarized in Table 5.

Figure 15 shows the variation of  $^{222}\text{Rn}$  concentration for the full duration of the pressure dependence experiment. Additionally, Figure 16 shows four individual regions for four different pressure values listed above.  $^{222}\text{Rn}$  concentration in the plots in Figure 16 is corrected for exponential decay, by multiplying the concentration with the exponential law (using the half-life period for  $^{222}\text{Rn}$  of 3.82 days). This is done for easier comparison with the experiment at atmospheric pressure, and to show that this decay obeys the exponential law.

Operation	Date	Days elapsed [d]
Stop circulation pump (MFC = 0.0 SLM)	9/30/2020 15:36	0.65
Bake the system	9/30/2020 15:37 – 17:12	0.65 – 0.72
Start circulation pump (MFC = 0.4 SLM)	9/30/2020 17:12	0.72
Bypass radon source	9/30/2020 17:24	0.725 = t <sub>0</sub>
Lower pressure to 0.08 MPa	10/1/2020 17:35	1.73
Turn on cold trap refrigerator	10/2/2020 16:05	2.67
Turn off cold trap refrigerator	10/5/2020 13:16	5.55
Lower pressure to 0.06 MPa	10/6/2020 13:22	6.56
Turn on cold trap refrigerator	10/7/2020 12:47	7.53
Turn off cold trap refrigerator	10/9/2020 16:56	9.71
Lower pressure to 0.04 MPa	10/12/2020 10:53	12.45
Turn on cold trap refrigerator	10/13/2020 12:02	13.50
Turn off cold trap refrigerator	10/15/2020 11:58	15.50
Lower pressure to 0.03 MPa	10/16/2020 17:07	16.71
Turn on cold trap refrigerator	10/19/2020 17:47	19.74
Turn off cold trap refrigerator	10/23/2020 17:27	23.73

Table 5: Operations carried out in the absolute pressure dependence experiment for ACF in CF<sub>4</sub>. Here, MFC is the mass flow controller.

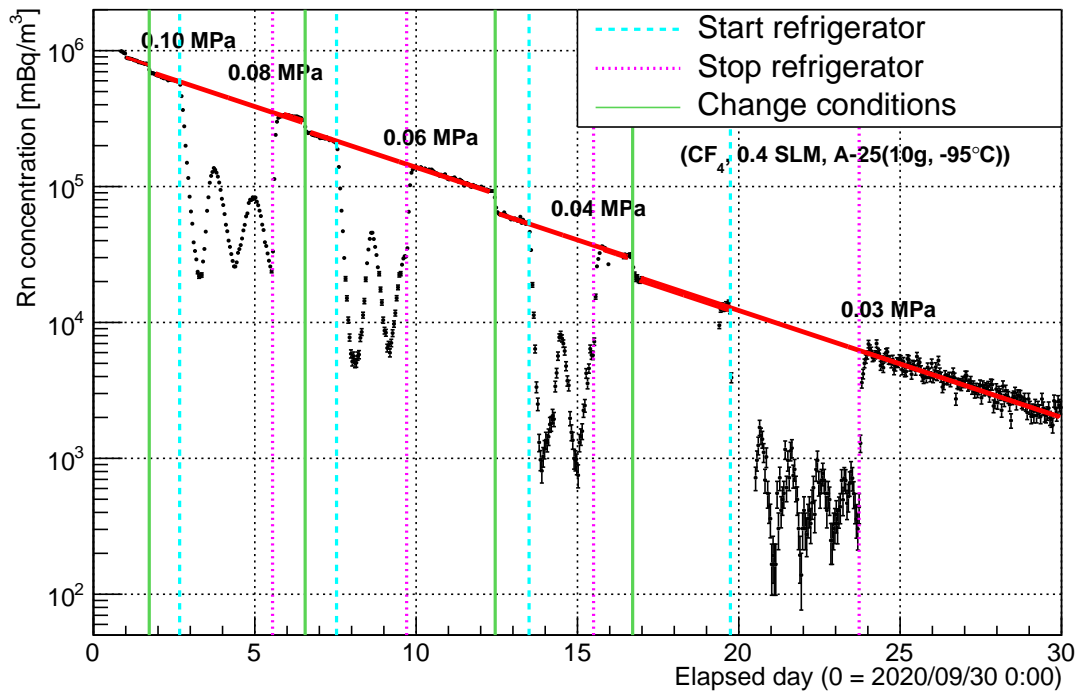
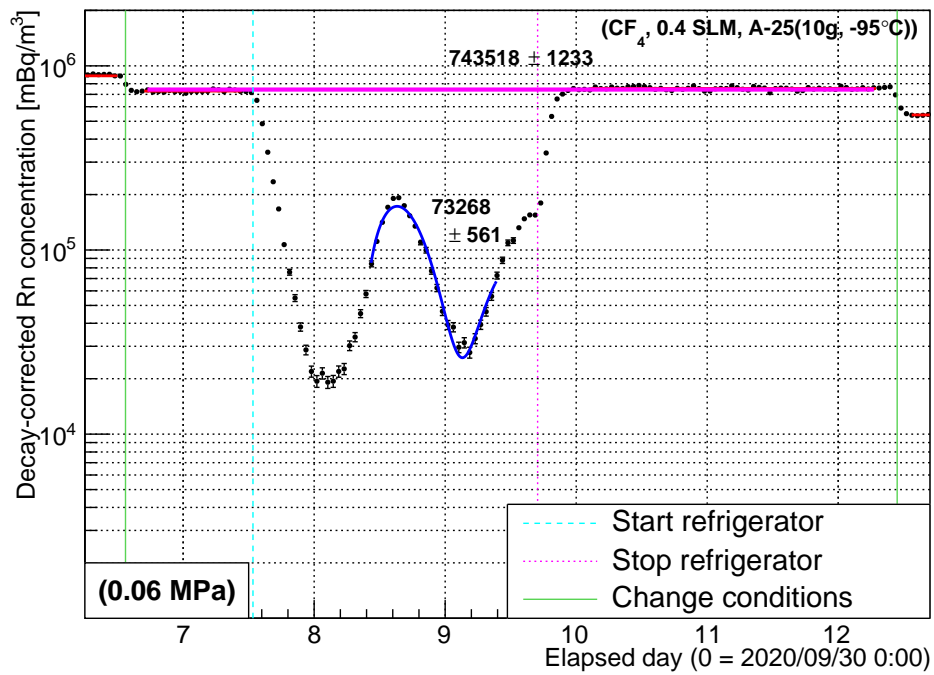
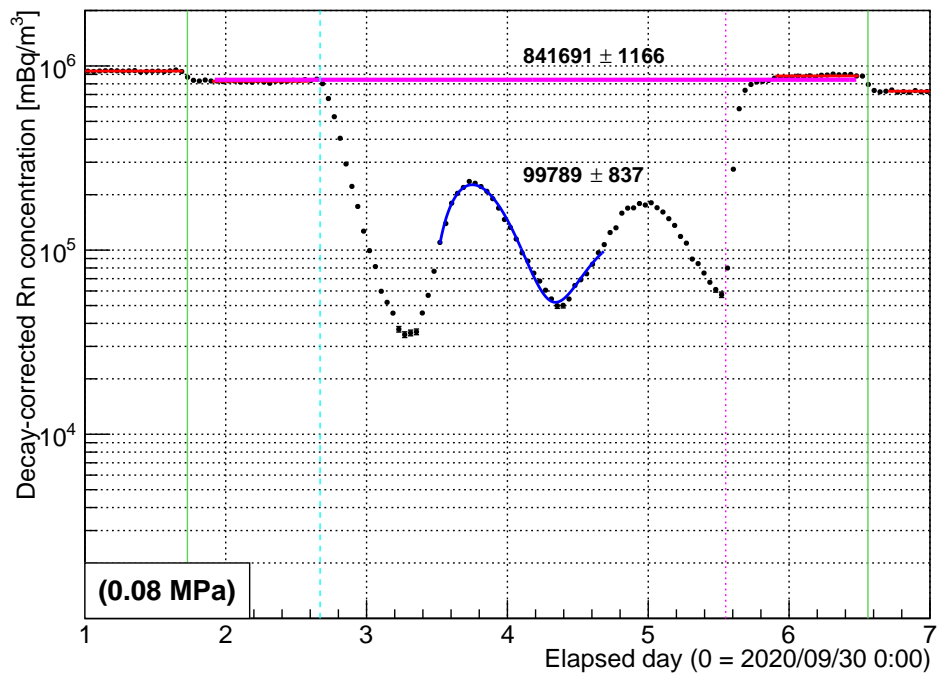


Figure 15: Variation of  $^{222}\text{Rn}$  concentration with pressure, with different operation times shown with vertical lines. The system pressure was lowered four times (pressure values written in black) and radon adsorption efficiency measured for ACF at each pressure level. In total, five periods of  $^{222}\text{Rn}$  decay were fitted, with each fit shown in red. The experimental conditions are written at the top right, where A-25 is the type of ACF used.



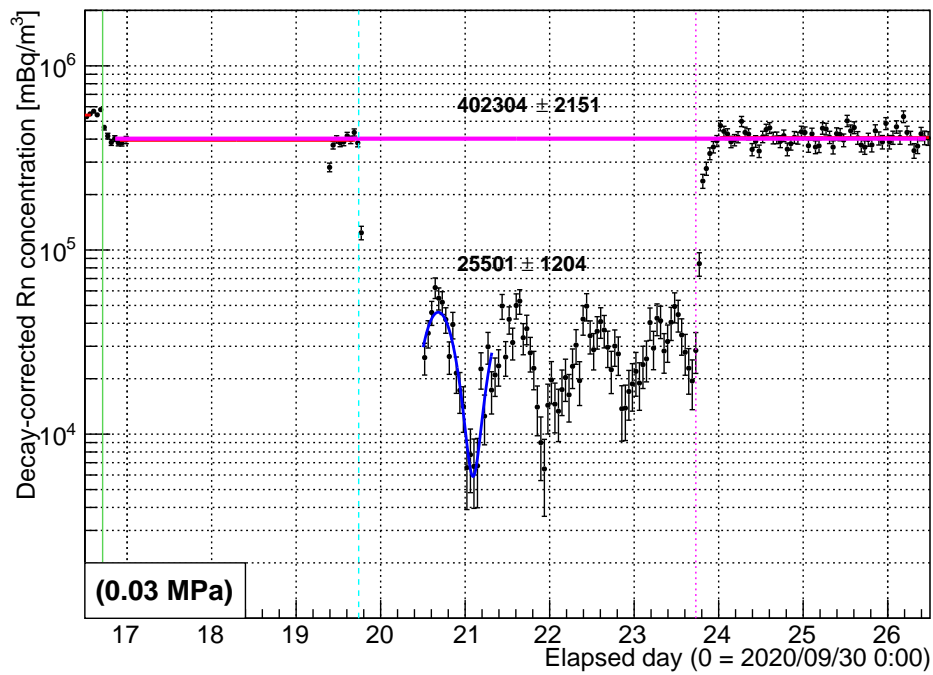
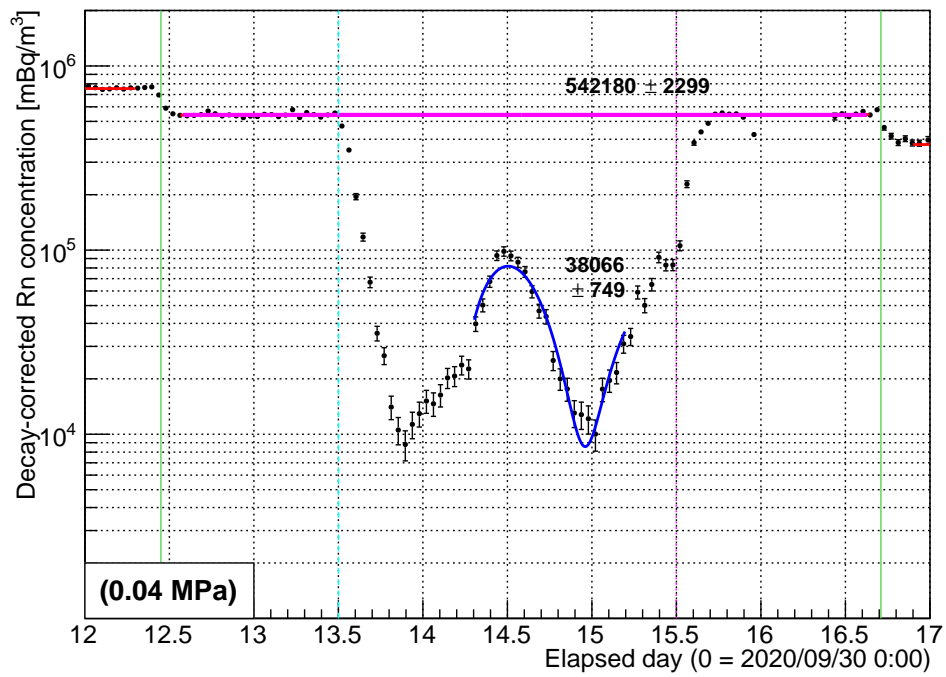


Figure 16: Decay-corrected  $^{214}\text{Po}$  count at four different pressure values in the adsorption efficiency experiment using  $\text{CF}_4$  gas. Operation times are shown with vertical lines and operations are explained in the legend in Figure 15, along experimental conditions at the top.

We have fitted the oscillatory parts according to method (2) in Sect. 5.3 and determined  $C_{\text{adsorbed}}$  for the four regions shown in Figure 16, and performed constant fits in the “off phases” for the same four regions to obtain  $C_{\text{off}}$ . Their relation, calculated as in Eq. (6) (this time accounting for the decay), is the  $^{222}\text{Rn}$  adsorption efficiency. Figure 17 and Table 6 show this efficiency for the five regions analyzed (including the adsorption efficiency at atmospheric pressure).

The adsorption efficiency at 0.03 MPa is  $93.7 \pm 0.3(\text{stat.}) \pm 3.9(\text{syst.})\%$ . The results suggest that the  $^{222}\text{Rn}$  adsorption efficiency has an inverse relationship with the pressure. This was also shown to be the case for Xe gas [30]. From this, it can be seen that at pressures lower than atmospheric pressure, ACF retains the ability to adsorb Rn in  $\text{CF}_4$ .

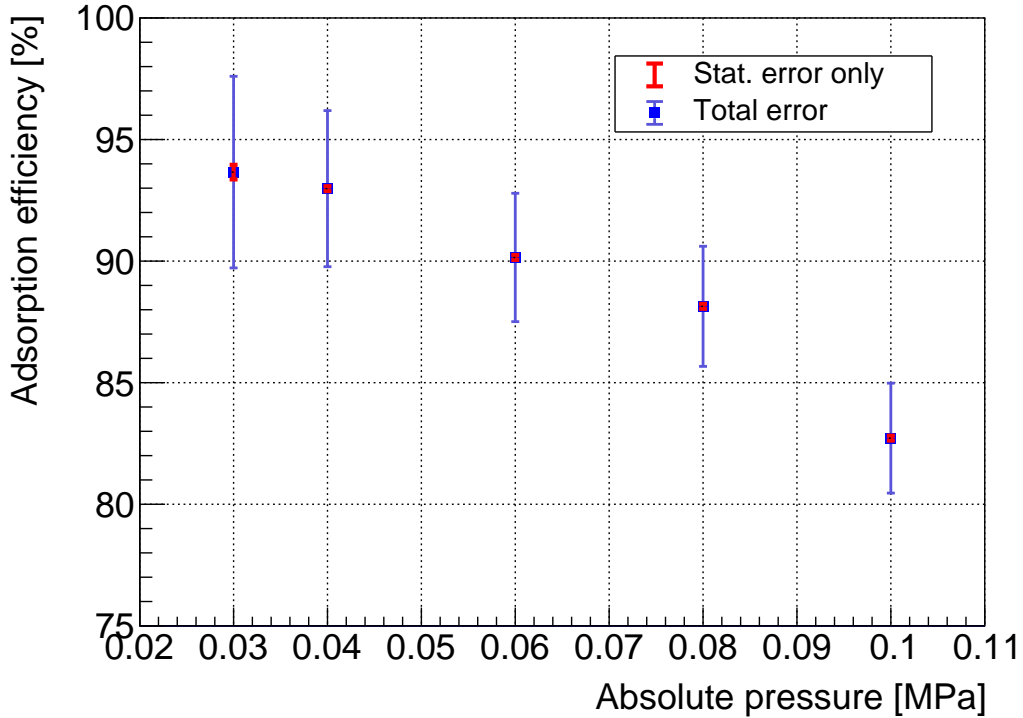


Figure 17:  $^{222}\text{Rn}$  adsorption efficiency of ACF in  $\text{CF}_4$  at  $-95^\circ\text{C}$  as a function of absolute pressure. The vertical error bars in red are statistical error only. The vertical error bars in blue include statistical and systematic uncertainties summarized in Table 7.

Since measurements in this experiment are performed one after another, it is expected that residual Rn exists in the trap, and this results in the different Rn concentrations before and after the adsorption phase. To take this into account, for each pressure level,  $^{222}\text{Rn}$  concentration was fitted as one weighted fit of two stable regions — the “off phases” before and after the “adsorption phase”. Note that there is no “bypass phase” this time, as the refrigerator was connected during the whole pressure dependence experiment. Results from separate fits of these two regions show that there is a difference in concentration between the before and after “off phases”. This difference ranges from  $-2.1\%$  (at 0.03 MPa)

to +4.9% (at 0.08 MPa). Propagating this difference to the uncertainty on the adsorption efficiency resulted in a range from  $-0.23\%$  (at 0.08 MPa) and  $+0.58\%$  (at 0.08 MPa). We have included this as a systematic uncertainty for adsorption efficiency in Table 7.

Absolute pressure [MPa]	Adsorption efficiency
0.10	$82.7 \pm 0.09(\text{stat.}) \pm 2.3(\text{syst.})\%$
0.08	$88.1 \pm 0.10(\text{stat.}) \pm 2.5(\text{syst.})\%$
0.06	$90.1 \pm 0.08(\text{stat.}) \pm 2.6(\text{syst.})\%$
0.04	$93.0 \pm 0.14(\text{stat.}) \pm 3.2(\text{syst.})\%$
0.03	$93.7 \pm 0.30(\text{stat.}) \pm 3.9(\text{syst.})\%$

Table 6:  $^{222}\text{Rn}$  adsorption efficiency of type A-25 ACF at pressures 0.10 MPa and lower

## 5.5 Systematic uncertainties

Next we estimated the systematic uncertainties on the adsorption efficiency. Since the experimental setup used in Ref. [30] is similar, we have inherited a  $\pm 2.0\%$  reproducibility uncertainty. We also had an accuracy uncertainty of the analog pressure gauge of  $\pm 0.001$  MPa, resulting in a pressure uncertainty between  $\pm 1.0\%$  (at 0.10 MPa) and  $\pm 3.3\%$  (at 0.03 MPa). A summary of the systematic uncertainties on the  $^{222}\text{Rn}$  adsorption efficiency is shown in Table 7. We have also included the uncertainty associated with the choice of a fitting region.

To estimate the systematic uncertainty associated with the choice of a fitting region, we performed two additional fits: we contracted and expanded the fitting region symmetrically, which gave us regions with less and more datapoints respectively. From this analysis, we obtained a systematic uncertainty between  $+0.3\%$  (at 0.04 MPa) and  $-10.0\%$  (at 0.03 MPa), which is listed in Table 7.

As an example of this estimation, graphs of the oscillation pattern of  $^{222}\text{Rn}$  concentration at 0.10 MPa and 0.03 MPa are shown in Figure 18. For these two regions, each graph shows three fits defined above. Datapoints closest to the middle red line at the approximate start and end of a period were selected as the first and last points, respectively, for the 1 period fit. The  $G$  parameters from each fit are shown in the plot. In the case of 0.03 MPa, the uncertainties of the  $G$  parameters were:

$$\begin{aligned} (24760 - 25501) / 25501 \cdot 100 &= -2.9 [\%] \\ (27879 - 25501) / 25501 \cdot 100 &= +9.3 [\%] \end{aligned} \tag{7}$$

These uncertainties were used as  $^{222}\text{Rn}$  concentration uncertainties. For the systematic uncertainties on  $^{222}\text{Rn}$  adsorption efficiency, we propagated these errors using Eq. (3), and obtained  $-0.18\%$  and  $+0.59\%$  for 0.03 MPa.

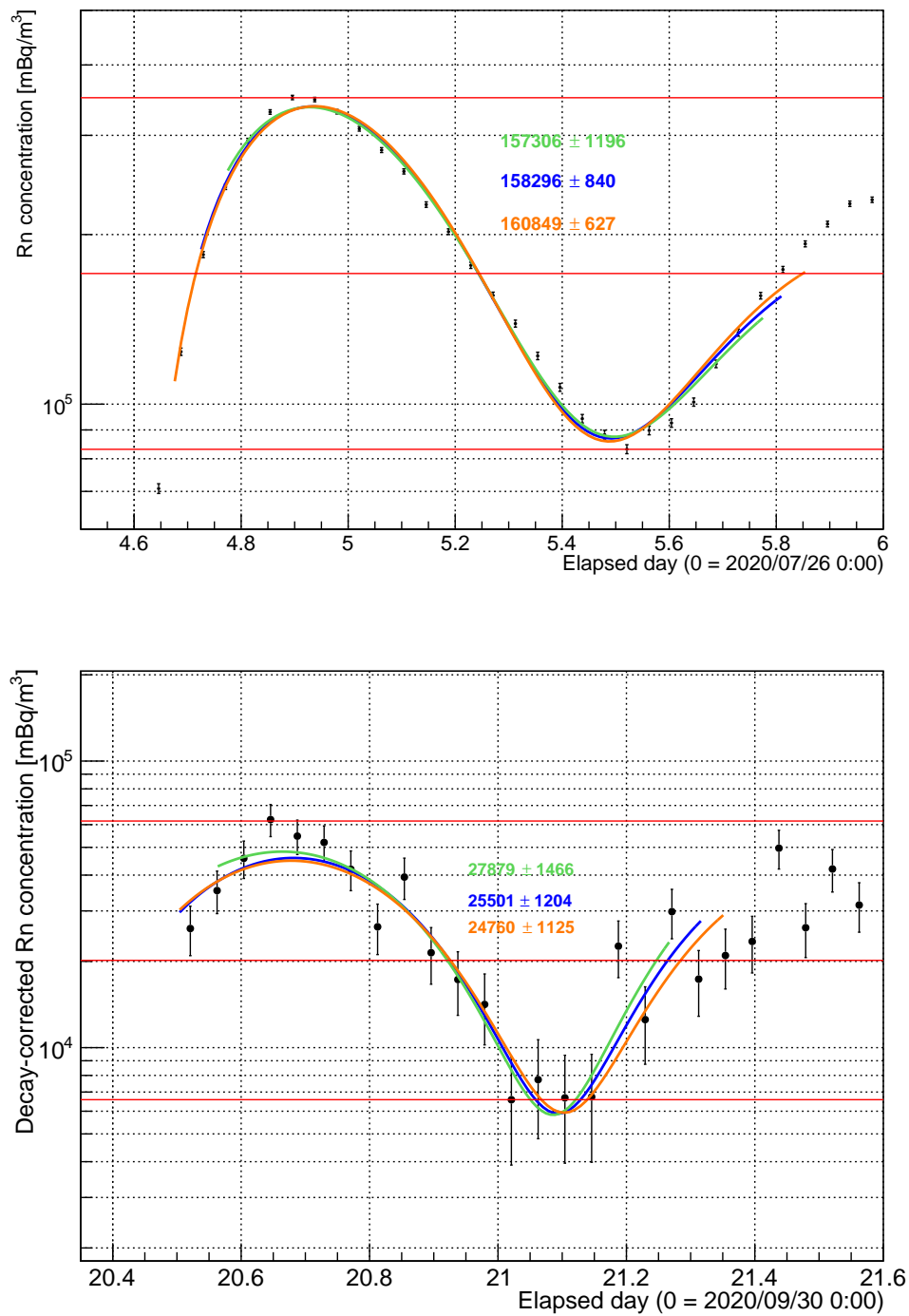


Figure 18: Three fits of the  $^{222}\text{Rn}$  concentration: approx. 1 osc. period (blue),  $\sim 1$  osc. period - 1 datapoint at both ends (green),  $\sim 1$  osc. period + 1 datapoint at both ends (orange), at 0.10 MPa (top) and 0.03 MPa (bottom). The obtained values of the  $G$  parameters are written in the center.

Cause	Uncertainty [%]
Accuracy of pressure	0.10 MPa: $\pm 1.00$
	0.08 MPa: $\pm 1.25$
	0.06 MPa: $\pm 1.67$
	0.04 MPa: $\pm 2.51$
	0.03 MPa: $\pm 3.33$
Reproducibility	$\pm 2.00$
Fitting region choice (method (2) only)	0.10 MPa: +0.28 and $-0.11$
	0.08 MPa: +0.43 and $-0.06$
	0.06 MPa: +0.37 and $-0.01$
	0.04 MPa: +0.14 and $-0.16$
	0.03 MPa: +0.59 and $-0.18$
Accuracy of the weighted fit ( <i>Sect 5.4 only</i> )	0.08 MPa: +0.58 and $-0.23$
	0.06 MPa: +0.14 and $-0.19$
	0.04 MPa: +0.04 and $-0.01$
	0.03 MPa: +0.13 and $-0.09$

Table 7: Systematic uncertainties on the  $^{222}\text{Rn}$  adsorption efficiency in  $\text{CF}_4$ .

## 6 Discussion and results

### 6.1 Calibration factor's dependence on absolute humidity

We would like to now present our speculation regarding the difference in absolute values of the calibration factor for different carrier gases. For this, consider the Lennard-Jones potential approximation, which is widely used in molecular physics. In the Lennard-Jones approximation, the  $\sigma$  parameter correlates with the separation distance, at which the attractive force between two molecules becomes 0, and thus represents the molecule size. Table 8 summarizes the  $\sigma$  parameters for different carrier gases mentioned in this study.

Gas type	$\sigma$ parameter [nm]	Rn adsorption efficiency [%]	Conditions
Ar	0.340–0.346 [40]	$98.3 \pm 0.1(\text{stat.}) \pm 0.2(\text{syst.})$	1.3 SLM, 0.1 MPa [30]
Air	0.352–0.369 [40]	$97.9 \pm 0.1(\text{stat.}) \pm 0.2(\text{syst.})$	0.9 SLM, 0.1 MPa [30]
Xe	0.396–0.410 [40]	$27.8 \pm 0.2(\text{stat.})_{-5.5}^{+2.0}(\text{syst.})$	0.14 SLM, 0.1 MPa [30]
Rn	0.417–0.421 [41]	–	–
CF <sub>4</sub>	$\sim 0.470$ [40]	$82.7 \pm 0.1(\text{stat.}) \pm 2.3(\text{syst.})$	0.4 SLM, 0.1 MPa

Table 8:  $\sigma$  parameters of the Lennard-Jones potential for different gases and Rn adsorption efficiency. CF<sub>4</sub> is the result presented in Sect. 4 of this paper.

Comparing the cases where the applied high voltage is  $-2.0$  kV (Figure 8), we can see that the calibration factor for CF<sub>4</sub> is about half the calibration factor of the other gases. This could be explained by the difference in  $\sigma$  parameters for the Lennard-Jones potential. Out of the gases for which the calibration factor's humidity dependence was explored so far, the CF<sub>4</sub>'s  $\sigma$  parameter is the largest ( $\sim 0.470$  nm), since CF<sub>4</sub> is a polyatomic molecule. On the other hand, as previously discussed, some Po ions that are drifting towards the photodiode in the detector's volume have a non-zero chance to scatter off the carrier gas molecules (as well as the water molecules mixed within the gas). Having scattered, they undergo neutralization and don't reach the photodiode surface, resulting in a lower count rate. Therefore, it could be speculated that the calibration factor depends also on the  $\sigma$  parameter of the gas type employed.

### 6.2 Pressure dependence of calibration factor

During the pressure dependence experiment of the adsorption efficiency of ACF, we have also calculated the pressure dependence of the calibration factor of the detector.

In this experiment, we varied the pressure in the system throughout a 1-month long decay experiment. During this time, the radon source was separated from the system, as in the concentration dependence experiment (Sect. 4.3). The variation of  $^{222}\text{Rn}$  concentration for the whole period is shown in Figure 15. If we assume that radon concentration is proportional to the system pressure, we can calculate the amount by which measured radon concentration differs from the expected drop with pressure.

To find the pressure dependence factor, we first calculated the ratios of the form  $N = \frac{C_{off}(n \text{ MPa})}{C_{off}(0.10 \text{ MPa})}$  (where  $C_{off}$  is the  $^{222}\text{Rn}$  concentration during the refrigerator's off phase) from the exponential coefficients in their fitting functions. Here,  $n$  stands for 0.08, 0.06, 0.04 or 0.03. The concentration values used in this calculation are the decay-corrected values (presented in Figure 16). We then divided this ratio by the pressure level ( $n$ ) in MPa to find how much  $^{222}\text{Rn}$  concentration exceeds the expected concentration at a given pressure level:  $A = \frac{N \cdot 0.10 \text{ MPa}}{n \text{ MPa}}$ . If the radon gas is reduced in the same proportion as carrier gas,  $A$  should equal 1. These quantities are shown in Table 9 as  $N$  and  $A$ , respectively.

We can see that, with the exception of the 0.03 MPa pressure level, the calibration factor for an 80 l radon detector seems to have an additional dependence factor that increases with a decrease in pressure. This is not entirely consistent on its own, however, as there may be other factors that influence the  $^{222}\text{Rn}$  concentration throughout the experiment. One of these factors is the nature of the pressure dependence experiment, which allowed some non-negligible amount of  $^{222}\text{Rn}$  to be adsorbed in the trap even after turning off the refrigerator. Analysis assumes that the proportion of radon remaining in the trap is constant at every measurement, but in the case it is dependent on pressure, the pressure dependence of the calibration factor will also change. It is also necessary to consider the influence of the concentration dependence described in Sect. 4.3. The analysis in this study assumes that there is no concentration dependence.

Using only the data measured in this study, it is not possible to separate the described dependencies. In order to evaluate the pressure dependence of the calibration factor without these dependencies, a system without the ACF trap must be used, like the one employed in Sect. 4. Then, at each pressure level, after a measurement the pressure needs to be returned once to atmospheric pressure and the radon source connected in circulation. That is because it is necessary to make every measurement in an identical state.

### 6.3 Radon adsorption efficiency of ACF

It can be speculated, that when the  $\sigma$  parameter for particles of the carrier gas is close to the  $\sigma$  parameter of  $^{222}\text{Rn}$ , a significant part of pores in the ACF will have these carrier gas particles adsorbed instead of  $^{222}\text{Rn}$ . This can be seen from the significantly low Xe adsorption rate in Table 8.

The obtained values for Rn adsorption efficiency in  $\text{CF}_4$  (Figure 17) could be explained by focusing on the inter-molecular interaction of gases near the surface of the ACF. As summarized in Table 8, Xe gas has the lowest  $^{222}\text{Rn}$  adsorption efficiency. This is possibly due to the fact that a considerable part of  $^{222}\text{Rn}$  atoms never has a chance to be adsorbed,

Absolute pressure [MPa]	$N$ (concentration ratio)	$A$ (pressure dependence factor)
0.10	1.000	1.000
0.08	0.919	1.149
0.06	0.812	1.353
0.04	0.592	1.480
0.03	0.440	1.467

Table 9:  $^{222}\text{Rn}$  concentration ratio and pressure dependence factor at pressures 0.10 MPa and lower

as they are superseded by Xe atoms, which have the closest Lennard-Jones  $\sigma$  parameter to  $^{222}\text{Rn}$ , and hence a suitable size for adsorption.

On the other hand, the amplitude of the oscillations at the start of adsorption also varies with different carrier gases. Comparing to results from [30], we can see that  $\text{CF}_4$  has the greatest amplitude out of the sample (Figure 14 and 15). This is hypothesized to be related to the Lennard-Jones  $\sigma$  parameter: a molecule with a large  $\sigma$  parameter is more likely to push an already residing molecule (in this case  $^{222}\text{Rn}$ ) out of a pore. This pattern is unlikely to occur for smaller sized molecules: small sized molecules will simply act as a diffusion medium. As we can see from their  $\sigma$  parameter in Table 8, purified air and Ar gas are such molecules.

## 7 Conclusion

CF<sub>4</sub> gas is widely used for particle detection in the field of particle physics because of its properties. We have evaluated the calibration factor for an 80 liter <sup>222</sup>Rn detector and analyzed its dependence on absolute humidity for the case of CF<sub>4</sub>. We have found a dependence on absolute humidity, which is described by the function  $C_F(AH) = -0.44\sqrt{AH} + 0.90$ , where  $C_F$  is the calibration factor defined in Sect. 4.1.2. Its value was found to be about the same as the calibration factor for Xe gas, and about half the calibration factor for Ar gas and purified air, for  $AH$  below  $10^{-2}$  g/m<sup>3</sup>,  $-2.0$  kV applied.

In Sect. 5, we have successfully employed ACF inside of a cold trap to evaluate its Rn adsorption efficiency in CF<sub>4</sub>. It was found to be  $82.7 \pm 0.1(\text{stat.}) \pm 2.3(\text{syst.})\%$  at 0.10 MPa (against room temperature adsorption at  $+25^\circ\text{C}$ ). For pressures lower than atmospheric pressure, namely between 0.10 MPa and 0.03 MPa, we have seen that it similarly increases with a decrease in pressure, up to  $93.7 \pm 0.3(\text{stat.}) \pm 3.9(\text{syst.})\%$  at 0.03 MPa. As these values are around 90%, we have therefore shown that ACF is a good candidate for use in a radon trap, specifically in the NEWAGE experiment, where the adsorption efficiency of the current trap was also evaluated at approximately 90%. Although the ratio of detector volume to the amount of the adsorbent used was larger than in this study, the efficiency results of this study are still comparable. In future, owing to ACF's convenient size, multiple ACF traps can be installed together to further reduce the radon level.

We have speculated that the lower adsorption efficiency, compared to other carrier gases, can be explained by a difference in the  $\sigma$  parameter in the Lennard-Jones potential.

We have also speculated that the calibration factor of an 80 l radon detector could depend on pressure, although this dependence is difficult to separate out in the current experiment, since there was a non-negligible amount of radon that stayed adsorbed in the trap each time the refrigerator was turned off, as well as there being a potential radon concentration dependence.

We have shown that at pressures lower than atmospheric pressure, ACF retains the ability to adsorb Rn in CF<sub>4</sub>. In this regard, it is a good candidate for use at experiments such as the NEWAGE experiment.

We have analyzed methods to employ in calculating the adsorption efficiency of an ACF, as well as related systematic uncertainties. In this study, we have confirmed that the sinusoidal adsorption behavior of an ACF trap can be fitted to good accuracy. The constant fitting parameter could then be used for the adsorbed concentration value in the calculation of adsorption efficiency.

## References

- [1] Y. Kotsar et al. "Evaluation of radon adsorption efficiency of activated carbon fiber using tetrafluoromethane". In: *Prog. Theor. Exp. Phys.* 2022 (Jan. 2022). ptac005. DOI: <https://doi.org/10.1093/ptep/ptac005>.

- [2] *Chandra X-ray Observatory's official website*. date last accessed December 21, 2021. URL: <https://chandra.harvard.edu/chronicle/0108/universe/>.
- [3] Jaan Einasto. "Dark matter". In: *Tartu Observatory, ICRANet* (2013). URL: <https://arxiv.org/abs/0901.0632>.
- [4] M. Kunz, S. Nesseris, and I. Sawicki. "Constraints on dark-matter properties from large-scale structure". In: *Phys. Rev. D* 94 (2016), p. 023510. ISSN: 2470-0029. DOI: <https://doi.org/10.1103/physrevd.94.023510>.
- [5] N. Aghanim et al. [Planck Collaboration]. "Planck 2018 results - VI. Cosmological parameters". In: *A&A* 641 (2020). DOI: <https://doi.org/10.1051/0004-6361/201833910>.
- [6] Vera C. Rubin and W. Kent Ford Jr. "Rotation of the Andromeda Nebula from a Spectroscopic Survey of Emission Regions". In: *Astrophys. J.* 159 (1970), p. 379. DOI: <https://doi.org/10.1086/150317>.
- [7] L. D. Bradley et al. "Discovery of a Very Bright Strongly-Lensed Galaxy Candidate at  $z \sim 7.6$ ". In: *Astrophys. J.* 678 (2008), p. 647. DOI: <https://doi.org/10.1086/533519>.
- [8] G. Jungman, M. Kamionkowski, and K. Griest. "Supersymmetric dark matter". In: *Phys. Rep.* 267 (1996), p. 195. DOI: [https://doi.org/10.1016/0370-1573\(95\)00058-5](https://doi.org/10.1016/0370-1573(95)00058-5).
- [9] A. Birkedal et al. "Little Higgs dark matter". In: *Phys. Rev. D* 74 (2006), p. 035002. ISSN: 1550-2368. DOI: <https://doi.org/10.1103/physrevd.74.035002>.
- [10] M. T. Arun, D. Choudhury, and D. Sachdeva. "Universal extra dimensions and the graviton portal to dark matter". In: *J. Cosmol. Astropart. Phys.* 2017 (2017), p. 041. ISSN: 1475-7516. DOI: <https://doi.org/10.1088/1475-7516/2017/10/041>.
- [11] E. Aprile et al. [XENON Collaboration]. "Dark Matter Search Results from a One Ton-Year Exposure of XENON1T". In: *Phys. Rev. Lett.* 121 (2018), p. 111302. DOI: <https://doi.org/10.1103/PhysRevLett.121.111302>.
- [12] T. Tanimori et al. "Detecting the WIMP-wind via spin-dependent interactions". In: *Phys. Lett. B* 578 (2004), p. 241. ISSN: 0370-2693. DOI: <https://doi.org/10.1016/j.physletb.2003.10.077>.
- [13] T. Hashimoto et al. "Development of a low- $\alpha$ -emitting  $\mu$ -PIC as a readout device for direction-sensitive dark matter detectors". In: *Nucl. Instrum. Meth. A* 977 (2020), p. 164285. DOI: <https://doi.org/10.1016/j.nima.2020.164285>.
- [14] A. Takada et al. "A very large area Micro Pixel Chamber". In: *Nucl. Instrum. Meth. A* 573 (2007). Proceedings of the 7th International Conference on Position-Sensitive Detectors, p. 195. ISSN: 0168-9002. DOI: <https://doi.org/10.1016/j.nima.2006.10.283>.
- [15] F. Sauli. "The gas electron multiplier (GEM): Operating principles and applications". In: *Nucl. Instrum. Meth. A* 805 (2016), pp. 2–24. DOI: <https://doi.org/10.1016/j.nima.2015.07.060>.

- [16] *UCL HEP group website*. date last accessed December 25, 2021. URL: <https://www.hep.ucl.ac.uk/darkMatter/>.
- [17] K. Hosokawa et al. “Development of a high-sensitivity 80 L radon detector for purified gases”. In: *Prog. Theor. Exp. Phys.* 2015 (2015). 033H01. ISSN: 2050-3911. DOI: <https://doi.org/10.1093/ptep/ptv018>.
- [18] K. Tai and N. Shindo. “Activated Carbon Fiber”. In: *Sen’i Gakkaishi* 49 (1993), P177. DOI: [https://doi.org/10.2115/fiber.49.5\\_P177](https://doi.org/10.2115/fiber.49.5_P177).
- [19] K. Abe et al. “Radon removal from gaseous xenon with activated charcoal”. In: *Nucl. Instrum. Meth. A* 661 (2012), p. 50. ISSN: 0168-9002. DOI: <https://doi.org/10.1016/j.nima.2011.09.051>.
- [20] M. Ikeda et al. “Adsorption and Desorption of Radon in Argon Gas, and the Development of Low Level Radon Concentration Measurement Method”. In: *Radioisotopes* 59 (2010), p. 29. DOI: <https://doi.org/10.3769/radioisotopes.59.29>.
- [21] S. Lindemann. In: *PhD thesis, Heidelberg University* (2013). <http://archiv.ub.uni-heidelberg.de/volltextserver/15725/>. DOI: <https://doi.org/10.1097/00004032-198802000-00001>.
- [22] K. Nakamura et al. In: *Prog. Theor. Exp. Phys.* 2015.4 (2015), 043F01. DOI: <https://doi.org/10.1093/ptep/ptv041>.
- [23] T. Ikeda et al. “Direction-sensitive dark matter search with the low-background gaseous detector NEWAGE-0.3b””. In: *Progress of Theoretical and Experimental Physics* 2021.6 (Apr. 2021), 063F01. DOI: <https://doi.org/10.1093/ptep/ptab053>.
- [24] M. Suzuki. “Activated carbon fiber: Fundamentals and applications”. In: *Carbon* 32 (1994), pp. 577–586. ISSN: 0008-6223. DOI: [https://doi.org/10.1016/0008-6223\(94\)90075-2](https://doi.org/10.1016/0008-6223(94)90075-2).
- [25] C. Mitsuda et al. “Development of super-high sensitivity radon detector for the Super-Kamiokande detector”. In: *Nucl. Instrum. Meth. A* 497 (2003), p. 414. DOI: [https://doi.org/10.1016/S0168-9002\(02\)01923-X](https://doi.org/10.1016/S0168-9002(02)01923-X).
- [26] In: *J. of Phys.: Conf. Series* 469 (2013), p. 12007.
- [27] M. Nemoto et al. “Development of High Sensitive Radon Detector with Electrostatic Collection”. In: *Radioisotopes* 46 (1997), p. 710. DOI: <https://doi.org/10.3769/radioisotopes.46.710>.
- [28] Y. Nakano et al. “Measurement of Radon Concentration in Super-Kamiokande’s Buffer Gas”. In: *Nucl. Instrum. Meth. A* 867 (2017), p. 108. DOI: <https://doi.org/10.1016/j.nima.2017.04.037>.
- [29] Y. Nakano et al. In: *Nucl. Instrum. Meth. A* 977 (2020), p. 164297. ISSN: 0168-9002. DOI: <https://doi.org/10.1016/j.nima.2020.164297>.
- [30] Y. Nakano et al. “Evaluation of radon adsorption efficiency values in xenon with activated carbon fibers”. In: *Prog. Theor. Exp. Phys.* 2020 (2020), 113H01. DOI: <https://doi.org/10.1093/ptep/ptaa119>.

- [31] D. O'Hagan. "Understanding organofluorine chemistry. An introduction to the C-F bond". In: *Chem. Soc. Rev.* 37 (2008), pp. 308–319. DOI: <https://doi.org/10.1039/b711844a>.
- [32] Myung-Kook Moon et al. "Low efficiency 2-dimensional position-sensitive neutron detector for beam profile measurement". In: *Nucl. Instrum. Meth. A* 538 (2005), p. 592. ISSN: 0168-9002. DOI: <https://doi.org/10.1016/j.nima.2004.09.020>.
- [33] C. Amsler et al. "The MUNU experiment, general description". In: *Nucl. Instrum. Meth. A* 396 (1997), pp. 115–129. DOI: [https://doi.org/10.1016/S0168-9002\(97\)00724-9](https://doi.org/10.1016/S0168-9002(97)00724-9).
- [34] E. Daw et al. "Spin-dependent limits from the DRIFT-IIId directional dark matter detector". In: *Astroparticle Physics* 35 (2012), pp. 397–401. ISSN: 0927-6505. DOI: <https://doi.org/10.1016/j.astropartphys.2011.11.003>.
- [35] S. Archambault et al. "Dark Matter Spin-Dependent Limits for WIMP Interactions on F-19 by PICASSO". In: *Phys. Lett. B* 682 (2009), p. 185. DOI: <https://doi.org/10.1016/j.physletb.2009.11.019>.
- [36] K. D. Chu and P. K. Hopke. "Neutralization kinetics for polonium-218". In: *Environmental Science & Technology* 22 (1988), p. 711. DOI: <https://doi.org/10.1021/es00171a016>.
- [37] Daiichi Kagaku Inc. *Humidity Calculation 1*. <https://www.daiichi-kagaku.co.jp/situdo/note/arekore08>. date last accessed May 1, 2021.
- [38] Ji ChoYeon, Seok ChoWoo, and San ChoiSang. In: *Materials and technology* 55 (2021), pp. 571–575. DOI: <https://doi.org/10.17222/mit.2021.145>.
- [39] *PureMax filter cartridges showcase website*. date last accessed December 25, 2021. URL: <https://www.sonaki.de/products/pmf-03p>.
- [40] J. O. Hirschfelder, C. F. Curtiss, and *Molecular Theory of Gases and Liquids* R. B. Bird. In: (Wiley, New York, 1954). p. 1110. DOI: 10.1002/pol.1955.120178311.
- [41] J. J. van Loef. "On the thermophysical properties of liquid radon-222". In: *Physica B+C* 103 (1981), p. 362. ISSN: 0378-4363. DOI: [https://doi.org/10.1016/0378-4363\(81\)90143-1](https://doi.org/10.1016/0378-4363(81)90143-1).